

DRAFT VERSION AUGUST 5, 2020

Typeset using L<sup>A</sup>T<sub>E</sub>X preprint style in AASTeX62

## Exploring the Mass Loss Histories of the Red Supergiants\*

ROBERTA M. HUMPHREYS<sup>1</sup>GRETA HELMEL<sup>1</sup>TERRY J. JONES<sup>1</sup>MICHAEL S. GORDON<sup>2</sup><sup>1</sup>*Minnesota Institute for Astrophysics, University of Minnesota, Minneapolis, MN 55455, USA*<sup>2</sup>*USRA-SOFIA Science Center, NASA Ames Research Center, Moffett Field, CA 94035, USA*

(Received; Revised; Accepted)

Submitted to AJ

## ABSTRACT

We report mid- to far-infrared imaging and photometry from 7 to 37 $\mu$ m with SOFIA/FORCAST and 2 $\mu$ m adaptive optics imaging with LBTI/LMIRCam of a large sample of red supergiants (RSGs) in four Galactic clusters; RSGC1, RSGC2=Stephenson 2, RSGC3, and NGC 7419. The red supergiants in these clusters cover their expected range in luminosity and initial mass from  $\approx 9$  to more than 25  $M_{\odot}$ . The population includes examples of very late-type RSGs such as MY Cep which may be near the end of the RSG stage, high mass losing maser sources, yellow hypergiants and post-RSG candidates. Many of the stars and almost all of the most luminous have spectral energy distributions (SEDs) with extended infrared excess radiation at the longest wavelengths. To best model their SEDs we use DUSTY with a variable radial density distribution function to estimate their mass loss rates. Our  $\dot{M}$  – luminosity relation for 42 RSGs basically follows the classical de Jager curve, but at luminosities below  $10^5 L_{\odot}$  we find a significant population of red supergiants with  $\dot{M}$  below the de Jager relation. At luminosities above  $10^5 L_{\odot}$  there is a rapid transition to higher mass loss rates that approximates and overlaps the de Jager curve. We recommend that instead of using a linear relation or single curve, the empirical  $\dot{M}$  – luminosity relation is better represented by a broad band. Interestingly, the transition

Corresponding author: Roberta Humphreys  
[roberta@umn.edu](mailto:roberta@umn.edu)

\* Based on observations obtained with (1) the NASA/DLR Stratospheric Observatory(SOFIA). SOFIA is jointly operated by the Universities Space Research Association, Inc.(USRA) under NASA contract NAS2-97001 and the Deutsches SOFIA Institut(DSI) under DLR contract 50OK 0901 to the University of Stuttgart, and (2) LMIR-Cam/LBTI on the Large Binocular Telescope(LBT) an international collaboration among institutions in the United States, Italy, and Germany.LBT Corporation partners include The University of Arizona on behalf of the Arizona university system; Istituto Nazionale di Astrofisica, Italy; LBTBeteiligungsgesellschaft, Germany, representing the Max-Planck Society, the Astrophysical Institute Potsdam, and Heidelberg University; The Ohio State University, and The Research Corporation, on behalf of The University of Notre Dame, University of Minnesota, and University of Virginia.

to much higher  $\dot{M}$  at about  $10^5 L_{\odot}$  corresponds approximately to an initial mass of 18–20  $M_{\odot}$  which is close to the upper limit for RSGs becoming Type II SNe.

*Keywords:* circumstellar matter — stars: individual (MY Cep) — stars: mass loss — stars: winds, outflows — supergiants

## 1. INTRODUCTION

For many years, the standard view of massive star evolution progressed from blue supergiant or O star to red supergiant to terminal explosion as a supernova. We now know that the evolution and eventual fate of massive stars depends not only on their initial mass, but also on mass loss and their mass loss histories. It has been acknowledged for some time that the most massive stars do not evolve to the red supergiant region due to post-main sequence enhanced mass loss. The observations suggest an upper limit to the initial mass of stars that become red supergiants, corresponding to  $\approx 40M_{\odot}$ . Thus, the majority of massive stars, those between 9 and 30 or 40  $M_{\odot}$ , will pass through the red supergiant stage, an important end product of stellar evolution.

Smartt (2009, 2015) has identified what he calls “the red supergiant problem,” the lack of Type II-P and Type II-L SNe progenitors, usually considered to be red supergiants (RSGs), with initial masses greater than 18  $M_{\odot}$ . Thus, the most luminous and most massive RSGs (18 – 30  $M_{\odot}$ ) would presumably end their lives some other way. The RSG stage is a high mass-losing stage. To what extent mass loss and their mass loss histories can affect the terminal state of the RSGs and their warmer counterparts is an open question. Even though the mass loss mechanism for RSGs is still debated, we can measure their mass loss from the thermal infrared emission from their circumstellar dust. Depending on their mass loss, they may evolve back to warmer temperatures becoming warm hypergiants, possibly LBVs, and even WR stars before the terminal explosion or possibly collapse directly to black holes. How they end their lives is pivotal for stellar evolution and the enrichment of the interstellar medium.

In a series of papers by Shenoy et al. (2013, 2015, 2016) and Gordon et al. (2018), we have demonstrated that we can map the geometry of the circumstellar ejecta and reconstruct the mass loss histories of the evolved warm and cool hypergiants over the past 1000 years using a combination of high spatial resolution near- and mid-infrared imaging and polarimetry over a wide range of wavelengths. In combination with SOFIA/FORCAST imaging at much longer wavelengths, we can extend their mass-loss histories to several thousand years. In Shenoy et al. (2016), hereafter Paper I, we mapped the cold dust in the mid- to far-infrared and discussed the mass loss histories of the famous hypergiants, VY CMa, IRC +10420 and  $\rho$  Cas, with some of the highest known mass loss rates. In our second paper, Gordon et al. (2018), hereafter Paper II, we extended our sample with SOFIA/FORCAST observations of three additional strong infrared and maser sources, NML Cyg, VX Sgr and S Per, plus two normal or more typical RSGs, T Per and RS Per.

Our two previous studies concentrated on individual stars, most with well-known strong infrared emission from dust and high mass loss rates. The extended circumstellar emission of the hypergiants, VY CMa and IRC 10420, revealed their complex mass loss histories, and many of the most luminous RSGs showed evidence for variable mass loss over the past thousand years or so, hinting at episodic high mass loss events. Although, it is well known that the RSG mass loss rate increases with

luminosity, it is not known if the stars evolve during the RSG stage becoming cooler, with more extended envelopes and higher mass-loss before the terminal state. To examine this question about red supergiant evolution, we have obtained mid- to far-infrared imaging with SOFIA/FORCAST and near-infrared adaptive optics imaging with LBT/LMIRCam of coeval samples of RSGs in Galactic clusters.

We have selected four clusters with numerous RSGs. *RSGC1* (Figer et al. 2006; Davies et al. 2008), *RSGC2* = Stephenson2 (Davies et al. 2007; Stephenson 1990) and *RSGC3* (Alexander et al. 2009; Clark et al. 2009) are massive clusters with remarkably large populations of RSGs and evolved stars. The fourth cluster is *NGC 7419* (Marco & Negueruela 2013) with five RSGs, one with a very late spectral type (MY Cep, M7 I) and high luminosity, plus a large number of confirmed B and Be-type members. The red supergiants in the clusters are presumably coeval with known distances and the same composition. They are thus an ideal population for comparing the stars’ mass loss histories with their derived parameters such as such as luminosity, spectral type, and initial mass at a fixed age and in a known environment.

In the next section we describe the observations and data reduction with SOFIA/FORCAST and LBT/LMIRCam. In §3 we briefly discuss our use of DUSTY (Ivezic & Elitzur 1997) and the determination of the mass loss rates. In §4 we describe the results for the four clusters. We discuss the mass-loss rate-luminosity relation for red suergiants and summarize our conclusions with respect to their evolutionary state §5, and in a brief final section we summarize our recommendations with respect to their mass loss rates.

## 2. OBSERVATIONS AND DATA REDUCTION

### 2.1. SOFIA/FORCAST:Mid- to Far- IR imaging (5 – 37 $\mu\text{m}$ )

The four clusters were observed with SOFIA/FORCAST during Cycles 5 and 6 in two independent programs; 05-0064 PI: Smith for RSGC1 and RSGC3 and 06-0089 PI: Humphreys for RSGC2 and NGC 7419. The observations are summarized in Table 1.

**Table 1.** SOFIA/FORCAST Observations

Cluster	Date	Filters	Program
RSGC1	2017 Aug 02	F056,F077,F111,F253,F315	05-0064
RSGC2	2018 Aug 29, 31	F077,F111,F197,F253,F315,F371	06-0089
RSGC3	2017 Aug 03, 07	F056,F077,F111,F253,F315	05-0064
NGC 7419	2018 Aug 28	F111, F315, F371 <sup>a</sup>	06-0089

<sup>a</sup>Reduced usable data (level 3 or 4) were not available for filters F077,F197,F253 for NGC 7419.

FORCAST is a dual-channel mid-IR imager covering the 5 to 40  $\mu\text{m}$  range. Each channel uses a  $256 \times 256$  pixel blocked-impurity-band (BiB) array and provides a distortion-corrected  $3'.2 \times 3'.2$  field of view with a scale of  $0''.768$  per pixel. FORCAST achieves near-diffraction limited imaging, with a PSF FWHM of  $\sim 3''.7$  in the longest filters.

Due to the complexities of most of the cluster fields with multiple sources a large chop throw was required. To mitigate coma effects, we used the asymmetric chop C2NC2 mode. With a much sparser

population and lower background contamination, NGC 7419 was observed in NMC mode. In NMC mode, the chop is symmetric about the optical axis of the telescope with one of the two chop positions centered on the target, and the nod is anti-parallel to this chop throw. C2NC2 is useful for large extended objects or, in the case of these RSG clusters, targets within crowded fields. In this mode, the chop throw is asymmetric, such that one chop position is centered on the optical axis (and the target) while the second (sky) position is off-axis. Rather than nodding, the telescope then slews to an offset position free of sources or significant background and the same chop pattern is repeated. Both of these SOFIA/FORCAST observing strategies offer the same imaging sensitivity and data quality, with NMC mode being much more efficient in terms of on-source telescope time.

We use the level 3 or 4 flux-calibrated images from the SOFIA/FORCAST pipeline which corrects for bad pixels, removes sky and telescope background emission and coadds the aligned and merged images. Aperture photometry was then measured using the open-source Astropy (Astropy Collaboration et al. 2013) photutils package with  $10''$  apertures. A larger  $15''$  aperture was used for selected stars such as MY Cep to include possible emission in their extended profiles. The photometry for each cluster is reported and discussed in §4. The images obtained in Cycle 6 in 2018 were adversely affected by the degradation of the FORCAST entrance window. This limited the usefulness of some filters, especially the shorter wavelength filters for NGC 7419.

The new FORCAST fluxes for the measured stars are given in the Appendix. The reported errors are from the measured uncertainty in the sky background annulus.

### 2.2. *Other Infrared Sources: Near- to Mid- IR Photometry (2 – 20 $\mu\text{m}$ )*

One of our goals with our SOFIA/FORCAST observations was to extend the available photometry to longer wavelengths to search for the presence of cooler circumstellar dust for a more complete picture of their mass loss histories. We combine our new long wavelength photometry from FORCAST with published fluxes from existing infrared surveys such as 2MASS (Skrutskie et al. 2006), *Spitzer*/IRAC Glimpse survey (Benjamin et al. 2003), WISE (Wright et al. 2010), MSX (Egan et al. 2001), and AKARI (Murakami et al. 2007) to produce the SEDs for the cluster members discussed here. Not all of the cluster stars were in the FORCAST field of view, but are included in our analysis using data from the above sources. Color-coded identification for the different sources for the photometry is used on the selected SEDs shown in the figures throughout this paper.

### 2.3. *LBT/LMIRCam: Adaptive Optics Near-IR Imaging (2 $\mu\text{m}$ )*

We also obtained high spatial resolution images of several of our program stars with LMIRCam (Skrutskie et al. 2010) with the LBTI (Hinz et al. 2016) using a single 8.4 m primary mirror of the Large Binocular Telescope (LBT). The focal plane scale was  $0.0106''$  per pixel and all images were made in the Ks ( $2.16 \mu\text{m}$ ) filter. The observing log is listed in Table 2 where the star used for the night’s point spread function (PSF) is given in column 2. The AO secondary was operating in natural guide star mode for all observations. The telescope guides or “locks-on” to the target which must be bright enough in the visual-red detector for this purpose. Consequently, many of the faint stars in these clusters, especially RSGC1, were not observed.

All of the PSF stars were observed with combinations of individual frame time and apparent brightness that resulted in images that did not contain saturated pixels. All of the program stars were overexposed to a varying degree to bring up the brightness at the target radii. The program stars divide roughly into two groups, those that were moderately overexposed and have usable data

starting at  $\sim 0''.1$  (group 1) and a group that were more heavily overexposed and have usable data starting at  $\sim 0''.5$  (group 2). these groupings are indicated in column 4 of Table 2.

An azimuthally averaged profile for the PSF star HD 216721 is shown in Figure 1 where the vertical axis is the ratio of the surface brightness in ADUs-per-pixel to the total ADUs for the stellar image. Clearly visible are the first three Airy rings at 0.09, 0.15 and 0.2 arcseconds. This star and GSC 04014-0230 were used as the PSF standard for stars in group 1. The PSF star observations for group 1 had very stable FWHM values, but there was some variation in the wings beyond  $0''.3$ , outside the region we are using.

The azimuthally averaged profile for GSPC S875-C is also shown in Figure 1, where the vertical axis is the same as for HD 216721. For this PSF star, only the region between  $0''.5$  and  $1''.0$  was used for the stars in group 2. For group 1, we will be investigating scattered light in the mass loss wind at radial distances of  $\sim 0''.1$ , about 300 AU at a distance of 3 kpc. For group 2, we will be investigating scattered light in the mass loss wind at radial distances of  $\sim 0''.7$ , about 4200 AU at a distance of 6 kpc. As a check on our PSF for group 2, direct comparison between radial profiles of stars in the frame and between frames in this group were compared. Only RSGC-02 showed any clear difference (an excess) from the other stars, or the PSF star.

**Table 2.** LMIRCam Observations at  $2.16 \mu\text{m}$

Target Star	PSF Star	Date	Group
N7419-B950(MY Cep)	HD 216721	2016 Oct 12	1
N7419-B139	HD 216721	2016 Oct 12	1
RSGC1-04	GSPC S875-C	2017 Apr 10	2
RSGC2-02	GSPC S875-C	2017 Apr 10	2
RSGC2-03	GSPC S875-C	2017 May 20	2
RSGC2-08	GSPC S875-C	2017 May 20	2
RSGC2-06	GSPC S875-C	2017 May 20	2
M1-s04 <sup>a</sup>	GSPC S875-C	2017 May 21	2
M1-s03 <sup>a</sup>	GSPC S875-C	2017 May 21	2
N7419-B696	GSC 04014-0230	2017 Oct 03	1

<sup>a</sup>These two RSGs from Masgomas-1 (Ramirez Alegria et al. 2012) were added to the LMIRCam program because they were bright enough for the AO guiding system.

The azimuthally averaged radial profile for each star observed with LMIRCam was computed and compared to the mean radial profile of the PSF standard observed on the same night (see Table 2). No 2D information on the sky was measured, only the mean radial profile. Four examples are shown in Figures 2 and 3, one each from group 1 and 2 described in §2.3 that had measurable extended emission, and one each in the two groups that did not. In all cases the vertical axis is the ratio of the amount of flux in a single pixel to the total flux from the star in the image. For highly saturated stars, the total flux was estimated by matching the stellar profile to the PSF at large radii ( $1.1 - 1.5''$ ), and using the PSF profile (which is unsaturated) to extrapolate to the total flux. Since errors in total flux only slightly influence the PSF subtraction, we did not make a comparison of total flux

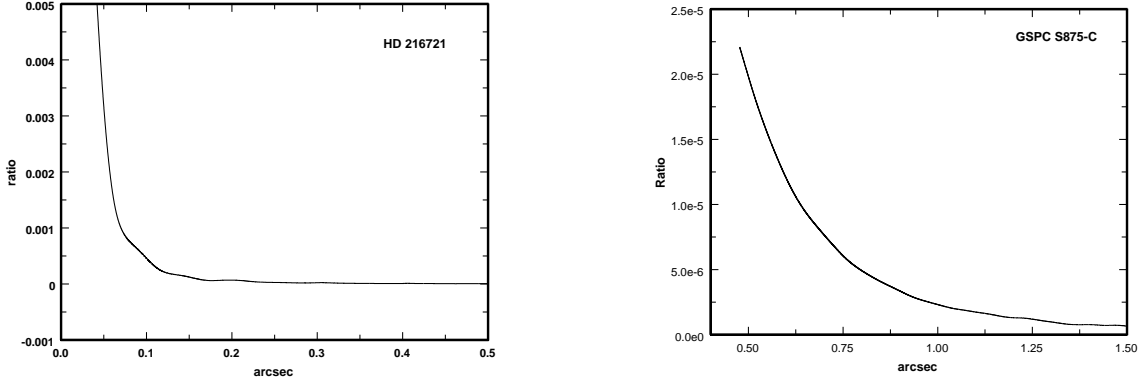


**Figure 1.** Left: Azimuthally averaged radial profile of the PSF star HD 216721. Vertical units are the ratio of the surface brightness (flux per pixel) to the total flux in the stellar image. Right: Azimuthally averaged radial profile of the PSF star GSPC S875-C. Vertical units are the ratio of the surface brightness (flux per pixel) to the total flux in the stellar image.

with 2MASS photometry. The major uncertainty in measuring net emission above the PSF profile is not raw signal-to-noise, as there is plenty of signal. Rather, systematic effects that can influence the width of the stellar profile, which dominates the systematic effects for group 1, and fitting the PSF at large radii, which dominates the systematic effects for group 2, are the primary sources of our estimate of the uncertainty.

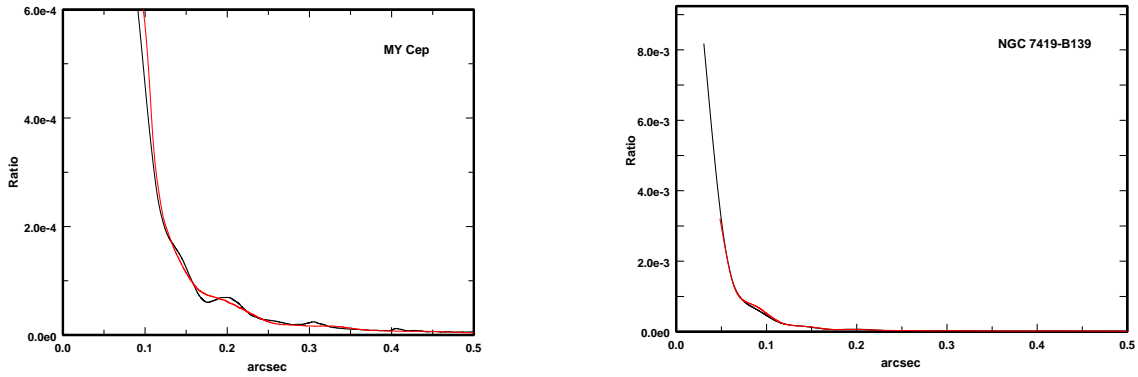


**Figure 2.** The averaged radial profile for MY Cep (B950) compared with a PSF standard. The vertical axis is the contrast ratio in flux per pixel divided by the total flux from the star. MY Cep is in group 1, and shows extended emission within a radius of  $0.1''$ , about 300AU. Right: Averaged radial profile for NGC 7419-B139 compared to a PSF standard. This star also in group 1 did not show any measurable extended emission.

### 3. DUSTY MODELING AND MASS LOSS

To estimate the mass-loss rates and determine the density distribution of the gas and dust, we use the DUSTY radiative-transfer code (Ivezic & Elitzur 1997) to model the observed SEDs similar to



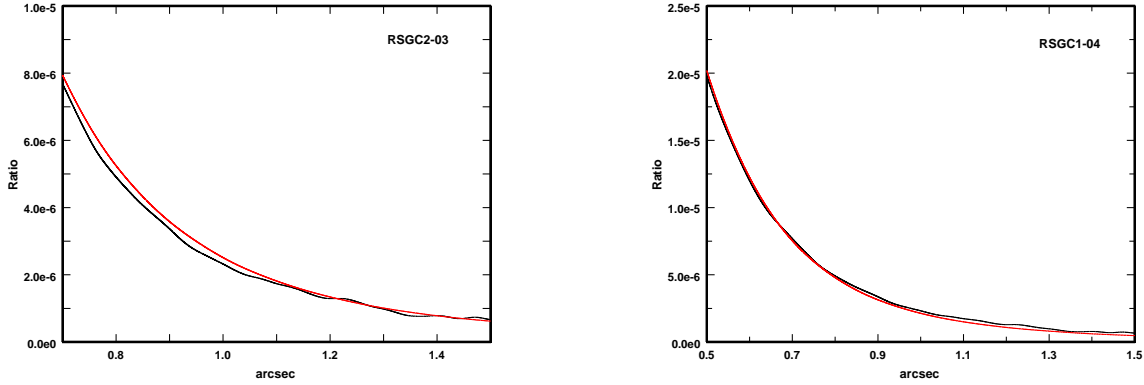


**Figure 3.** Left: Averaged radial profile for RSGC2-03 compared with a the PSF standard. The vertical axis is the contrast ratio in flux per pixel divided by the total flux from the star. This star is in group 2, and shows measurable extended emission. The stellar profile begins to enter the non-linear regime at radii less than  $0.6''$ . Right: Averaged radial profile for RSGC1-04 compared to a PSF standard. It shows no measurable extended emission.

our Papers I and II. DUSTY solves the one-dimensional radiative transfer equation for a spherically symmetric dust distribution. The input includes the optical properties of the dust, the chemistry, size of the grains, and a dust condensation temperature which sets the dust condensation radius,  $r_1$ . For the dust optical properties, we use the ‘cool’ circumstellar silicates (Ossenkopf et al. 1992) and assume that the grains follow an MRN size distribution,  $n(a) \propto a^{-3.5} da$  (Mathis et al. 1977) with  $a_{min} = 0.005 \mu\text{m}$  and  $a_{max} = 0.5 \mu\text{m}$ .

We generate a series of models for each star with an adopted stellar temperature initially corresponding to its spectral type when available, and a fixed shell extent ( $1000 r_1$ ). We chose the Planck curve option in DUSTY to fit the near- and mid -infrared fluxes instead of an atmospheric model. All but two of the red supergiants lack the usable visual photometry for the model fits. Together with the range in the published spectral types and scatter in the fluxes discussed later, we considered the Planck curve fits adequate for our purposes.

The dust condensation temperature is an important parameter in modeling the wind. Values in the literature vary from 700–1500 K (Cassarà et al. 2013) with a range of 700–1000 K for silicate-rich dust shells. In this work, we adopt a fixed dust condensation temperature of 1000 K for the temperature of the inner shell ( $T_{in}$ ) following Suh (2002) and consistent with observations of RSG dust shells (Rowan-Robinson & Harris 1982). We varied the optical depth  $\tau_v$  of the circumstellar material from 0.01 up to 5, but find that a realistic range for most of the stars in this study is  $\tau_v$  of 0.1 to 1. We also vary the density distribution function, which in DUSTY is modeled as a power law,  $\rho(r) \propto r^{-n}$ . An index of  $n = 2$  is for the standard constant mass-loss rate. An index less than that indicates a higher mass-loss rate in the past and a decline over the dynamical age. We initially adopted the constant mass loss density prescription with  $\rho(r) \propto r^{-2}$  and varied  $\tau_v$  to get a best fit SED. However, several stars with a large circumstellar excess radiation at long wavelengths required a less steep power law. In this paper we show the DUSTY fits for a constant mass-loss rate,  $n = 2$  and adopt a lower value of  $n$  for those stars with large excess radiation at the longest wavelengths.

### 3.1. The Mass-Loss Rate

If we assume a constant mass-loss rate over time and a uniform expansion velocity, the mass-loss rate is the familiar equation  $\dot{M}(t) = 4\pi r^2 \rho(r) v_{exp}$ . But for stars with a non-constant mass-loss rate ( $n \neq 2$ ), it is necessary to integrate the density distribution over the spatial extent of the shell. We discuss the derivation of the form of this equation based on the input from DUSTY for a non-constant mass loss rate in the Appendix. The mass loss rate for dust in  $\text{gm s}^{-1}$  is given by:

$$\dot{M} = \frac{M_{tot} V}{r_{max} - r_{min}} \sim \frac{16\pi}{3} \frac{n-1}{3-n} \sqrt{a_{max} a_{min}} \rho_d \frac{\tau}{Q_{eff}} r_{max}^{2-n} r_{min}^{n-1} v_{exp} \quad (1)$$

This is Equation A8 in the Appendix. For a constant mass-loss rate, with  $n = 2$ , this becomes:

$$\dot{M} \sim \frac{16\pi}{3} \sqrt{a_{max} a_{min}} \rho_d \frac{\tau}{Q_{eff}} r_{min} v_{exp} \quad (2)$$

To determine the combined mass loss rate from dust and gas we require a gas to dust ratio (g/d). Most values range from 100 to 200 in the Galaxy with a high of 500 suggested for the Large Magellanic Cloud (Van Loon et al. 1999). In our two previous studies (Shenoy et al. 2016; Gordon et al. 2018) we adopted a gas to dust ratio of 100. Here we use a g/d ratio of 200 (Decin et al. 2006; Maun & Josselin 2011) for Galactic RSGs for comparison with other recent work. We also assume the nominal expansion velocity of  $25 \text{ km s}^{-1}$ . Higher expansion velocities of  $35 - 40 \text{ km s}^{-1}$  are measured for the most luminous red supergiants with high mass-loss rates. The impact of these two adopted parameters on our mass-loss rates and conclusions is discussed in §5.

### 3.2. Model Profiles

DUSTY computes a model radial profile at a chosen wavelength as a function of the inner dust radius  $r_1$  that can be compared to our LMIRCam observations. Since our LMIRCam images can experience saturation effects at small radii and uncertainties in normalization at larger radii, we chose to measure the excess surface brightness at a specific radii, between these two limitations. The results are given in Table 3. Using the distances in Table 4, we converted the angular distance of these radii to the projected physical distance in AU.

For the three stars in Group 1, the DUSTY profile needs to be convolved with our best PSF for us to determine the model surface brightness for comparison with our observations. DUSTY does output a radial profile that includes the contribution from the central star, but we are interested in just the excess we find in flux above the PSF at a specific radius with our LMIRCam observations. The contribution from the star and the shell are additive in the convolution with the PSF and convolving the dust shell is equivalent to subtracting the PSF from the observed profile for comparison with the observed excess over the PSF for the program star. We take this approach to make the effect of the convolution easier to see, which is important for separating the thermal and scattered emission in the dust. This is illustrated in Figure 4 for MY Cep where the DUSTY model profile of the dust shell has been convolved with the PSF. Note that the model surface brightness at  $b = 4.1$  ( $r = 300 \text{ AU}$ ) is dominated by scattered light, but that blurring by the PSF brings in thermal emission from smaller radii. We can then correct our observed excess flux at that radii for blurring by the PSF. For the 7 stars in Group 2, the excess flux is measured at  $0.7''$ , and no convolution is necessary. In this case, a direct comparison of the DUSTY model (if there is one) with the observed excess (if any) can be made.



We have converted our excess flux (corrected for the PSF) for those stars with a measurable excess into a scattering optical depth using the method outlined in Shenoy et al. (2015). This can be directly compared with the DUSTY model visual optical depth at the same impact parameter  $b$  by converting  $\tau_V$  to  $\tau_{sca}$  at  $2.16 \mu\text{m}$ , using the dust parameters that were inputs to DUSTY. The observed and model scattering optical depths are given in Table 3, where column 3 is the measured scattering optical depth with LMIRCam, corrected for PSF smearing, and column 4 is the model output value from the DUSTY models in the following section.

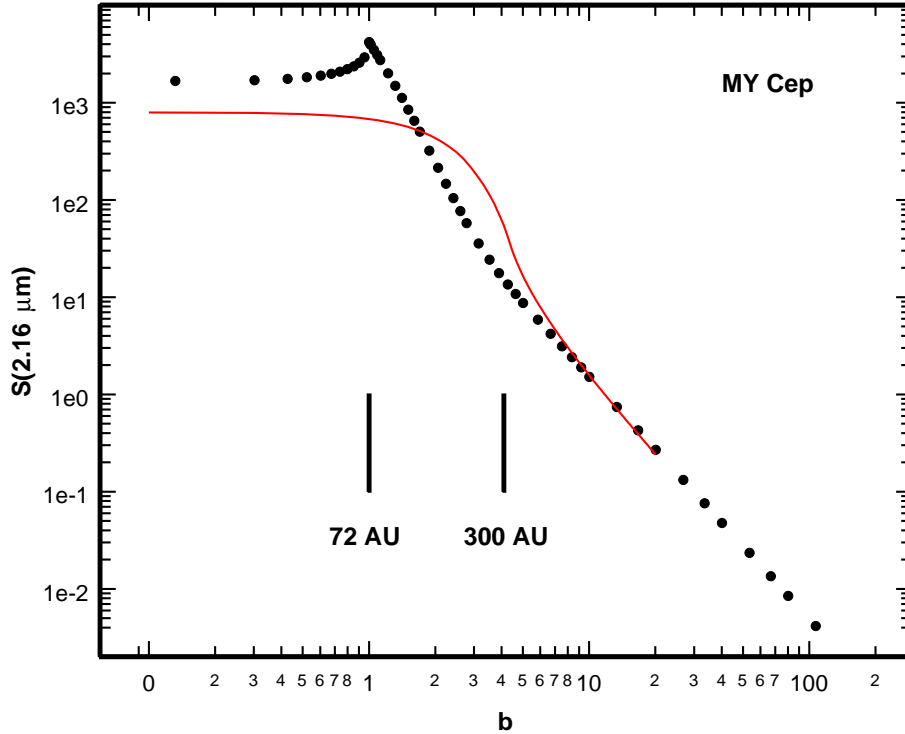


**Figure 4.** The projected radial profile of the DUSTY model dust shell at  $2.16 \mu\text{m}$  (black dots) as a function of the normalized impact parameter  $b$ . At  $r_1$ ,  $b = 1.0$ . The spike at  $b = 1$  ( $r_1 = 72 \text{ AU}$ ) is the inner edge of the dust shell. The break in the slope at  $b = 3$  is where the primary contribution to the surface brightness changes from thermal to scattered flux. The red line is the expected profile convolved with our PSF. The location of our LMIRCam flux measurement ( $0''.1$ ) is at  $300 \text{ AU}$ .

We were only able to measure excess flux for three of the program stars observed with LMIRCam, and only MY Cep has a solid detection. In the case of MY Cep, the observed optical depth is lower than predicted by the DUSTY model. This is likely due to the fact that DUSTY assumes isotropic scattering by the dust, but at  $2.16 \mu\text{m}$  the dust is highly forward scattering. Using our dust parameters and a wavelength of  $2.16 \mu\text{m}$ , the ratio of the scattered flux at a  $90 - 180^\circ$  scattering angle to the scattered flux at  $0^\circ$  (forward, away from the star) is calculated to be 0.25. We have not made a detailed integration down the line of sight at  $b = 4.1$  for MY Cep, but given the range of scattering

**Table 3.** Extended Scattered Emission

Star	radius (AU)	$\tau_{sca}$ 2.2 $\mu\text{m}$	$\tau_{sca}$ DUSTY
NGC 7419-B950	300	$0.035 \pm 0.005$	0.08
NGC 7419-B139	200	$< 0.02$	0.02
NGC 7419-B696	200	$0.015 \pm 0.005$	0.02
RSGC1-04	4500	$< 0.009$	-
RSGC2-02	4000	$< 0.009$	-
RSGC2-03	4000	$0.008 \pm 0.003$	0.0003
RSGC2-06	4000	$< 0.009$	0.00015
RSGC2-08	4000	$< 0.009$	0.0002
M1-s04	2500	$< 0.009$	-
M1-s03	2500	$< 0.009$	-

angles at different locations along this line of sight through the dust shell, the ratio between our observed flux and the model flux of 0.44 is reasonable.

For B696, the observed optical depth is comparable to the model prediction, suggesting a slight excess of emission at a 200 AU offset from the star. For group 2 stars, only RSGC2-03 had a measurable excess, albeit with  $S/N = 2.7$ . The observed scattering optical depth is significantly larger than the model prediction. If the observed value is real, then this star must have had a higher mass-loss episode about 1000 yrs ago, assuming a wind velocity of 20 km/s. Another possibility is that the dust in the outer shell of this star is scattering the diffuse interstellar radiation field within the cluster. None of the other stars in RSGC2 had measurable flux excesses, but their  $3\sigma$  upper limits on the observed scattering optical depth are too large for a careful comparison between stars.

The DUSTY models also provide predicted radial profiles at the longer wavelengths of our SOFIA FORCAST observations. We find that uncertainties in the reproducibility of the PSF between observations of standards and the program stars makes comparison between the FORCAST profiles and the DUSTY models highly uncertain. This is due to both variations in the SOFIA PSF and the large FWHM of 3 – 4" for the FORCAST images. Convolution of the DUSTY profiles with this large PSF results in very small enhancement to the stellar profile due to the presence of the dust shell.

#### 4. THE CLUSTERS

The adopted parameters for the four clusters, their distances, and foreground interstellar extinction are summarized in Table 4. The four clusters represent a significant range in their ages which is reflected in the properties of their red supergiant populations discussed in this section. For example, RSGC1, the youngest, has the most luminous RSG members and with the corresponding highest mass loss rates. Thus the three ‘‘RSG’’ clusters together provide a good sample for evaluating the evolutionary state of the red supergiants and the role of mass loss. NGC 7419, the closest, is in the middle of the age range, but has an interesting population with the very late-type RSG, MY Cep.

To estimate the luminosities of the red supergiants, we integrate their extinction-corrected SEDs with the adopted temperature from the DUSTY model fit to the observations. The greatest source of error in the derived luminosities is the uncertainty in the distance. NGC 7419 has a well-determined distance from Gaia parallaxes (Davies & Beasar 2019) at 3 kpc (+0.35, -0.29 kpc). This approxi-

mately 10% error in the distance leads to a 20% uncertainty in luminosity. The three ‘‘RSG’’ clusters are physically close on the sky, but much further away at the intersection of the Scutum-Crux spiral arm with the Galactic bar at approximately 6 kpc. Given their location they are more likely further away than significantly closer. In this work, we adopt the published distances with the estimated error which is typically  $\pm 1$  kpc corresponding to a 37% uncertainty in the derived luminosity. Other sources of error in the integrated SED are the adopted temperature, the interstellar extinction, and the fit to the observed fluxes. The combined errors are discussed for each cluster.

The uncertainty in the luminosity also enters into the calculation of the mass loss rate from the DUSTY model; specifically  $r_1$  in the DUSTY output where this parameter depends on  $L^{1/2}$  and on the adopted temperature in the DUSTY models.

To correct the observed fluxes for interstellar extinction we adopt the extinction corrections for the 2MASS data (Koorneef 1983) and follow the extinction law from Cardelli et al. (1989) for the longer wavelengths measured relative to  $A_K$ . The adopted correction for each cluster is discussed separately below and summarized in Table 4.

**Table 4.** Cluster Parameters Summary

Cluster	N(RSGs)	Dist(Kpc)	IS Ext(mag)	Mass $M_\odot$	Age(Myrs)	Refs <sup>a</sup>
NGC7419	5	$3.0 \pm 0.3$	$5.4(A_V)$	$5-10 \times 10^3$	$14 \pm 2^c$	1, 2, 3
RSGC1	14	$6.6 \pm 1$	$2.29(A_K)$	$2-4 \times 10^4$	7-12	4, 5
RSGC2	26	$5.8 \pm 1$	$1.32(A_K)^b$	$4 \times 10^4$	12-17	6
RSGC3	15	$6 \pm 1$	$1.5(A_K)$	$2-4 \times 10^4$	16-20	7, 8

<sup>a</sup>References: (1) Marco & Negueruela (2013), (2) Beasor & Davies (2018), (3) Davies & Beasor (2019), (4) Figer et al. (2006), (5) Davies et al. (2008), (6) Davies et al. (2007), (7) Alexander et al. (2009), (8) Clark et al. (2009)

<sup>b</sup>See text for RSGC2.

<sup>c</sup>Beasor et al. (2020) cite ages of  $20 \pm 1$  for NGC 7419 and  $7 \pm 2$  for RSGC1.

#### 4.1. NGC 7419

At 3kpc, NGC 7419 is relatively nearby with several published studies of its stellar content (Beauchamp et al. 1994; Subramanian et al. 2006; Joshi et al. 2008). It is best known for its five red supergiants in one cluster including the very late-type MY Cep (M7 -7.5 I ). The most recent study by Marco & Negueruela (2013) includes a comprehensive survey of its Be and B star population as well as the red supergiants.

To assess the total affect on the derived luminosities in addition to the error in the distance, we assume an uncertainty of  $\pm 100K$  in the adopted temperatures from the small range in the published spectral types for the RSGs in N7419 or  $\approx 10\%$  on the luminosity. The adopted  $A_V$  is derived from the normal B (non-Be) star members and although no error is quoted we adopt  $\pm 0.2$  mag or 4%. The combined error from the residuals to the SED fits for these stars is small corresponding to about 3% on the derived luminosity. Combining these errors with the distance, gives an uncertainty of 23% in luminosity and 14% in the mass loss rate.

MY Cep (B950) is especially interesting because it belongs to the rather rare late-type and relatively high luminosity RSGs; that is red supergiants with spectral types M4 to M5 and later. This group

includes stars like S Per, VX Sgr, NML Cyg and VY CMa with high mass loss rates, and extensive circumstellar dust and ejecta. All four are strong maser sources, and MY Cep is also source of OH, SiO, and H<sub>2</sub>O maser emission (Verheyen et al. 2012). MY Cep’s spectral energy distribution (SED) in Figure 5 clearly demonstrates the presence of circumstellar dust at the longer wavelengths. We ran DUSTY models with a range of  $\tau_v$  from 0.1 to 5. The model with  $\tau_v = 1$ , and  $T = 3000$  K is shown in the figure. It is clear that models with constant mass loss rate do not reproduce the far-infrared flux. Here we adopt  $n = 1.5$  indicating a higher mass-loss rate in the past. We integrate the observed best-fit SED fit from  $1 \mu\text{m}$  to  $40 \mu\text{m}$  together with a 3000 K Planck curve to fit the shorter wavelengths. The re-radiated flux from the circumstellar dust dominates the SED from  $8$  to  $40 \mu\text{m}$ . This gives a total luminosity of  $3.1 \times 10^5 L_\odot$  and a mass-loss rate of  $2.3 \times 10^{-5} M_\odot \text{ yr}^{-1}$  from Equation 1 (A8) with a gas to dust ratio of 200.

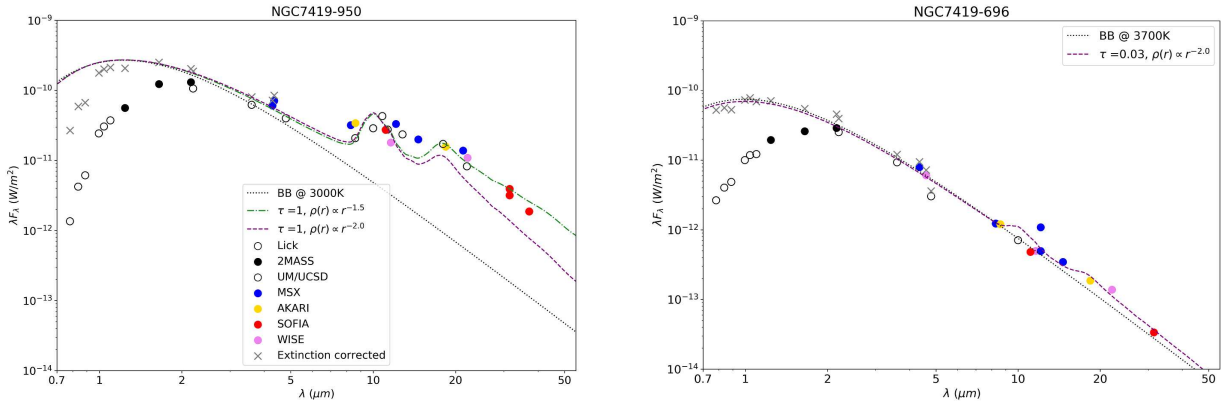


**Figure 5.** The SEDs for N7419-B950 (MY Cep), left, and B696, right, showing the observed (circles) and interstellar extinction corrected (tipped crosses) fluxes from different sources. The symbols are the same in each SED. The open circles are from Fawley & Cohen (1974). A Planck curve for the adopted temperature and the DUSTY model for different power laws are shown. MY Cep’s strong silicate emission feature and longer wavelength fluxes are best fit with a less steep power law ( $n = 1.5$ ). B696 has a weak dust emission if any and is fit with a low  $\tau_v$  and a constant mass-loss rate.

The four other RSGs are significantly less luminous and much earlier in spectral type. Their DUSTY models are consistent with a constant mass-loss rate with low  $\tau_v$ . The SEDs for B696, shown in Figure 5, B435, and B139 are best fit with a low  $\tau_v$  and a constant mass-loss rate. B921 has no long wavelength infrared excess and no evidence for circumstellar dust. We adopt an upper limit to its mass loss rate, based on the other three stars, in later discussion. Our results for the N7419 RSGs are summarized in Table 5. Note that B139 was not on the FORCAST frame.

Beasor & Davies (2018) have presented results for DUSTY models for the NGC 7419 RSGs. They treat the DUSTY models somewhat differently, allowing the dust condensation temperature ( $T_{in}$ ) to vary and assume a steady state/constant mass-loss rate density distribution for all of the stars. Their adopted temperatures are similar to ours. Despite the difference in the DUSTY modeling, and our adopted distance is also somewhat less than they used, the luminosities for the four less-luminous RSGs agree within our quoted errors although our  $\dot{M}$  are somewhat lower. The low errors on the luminosities cited by Beasor & Davies (2018) did not include the distance uncertainty (Davies & Beasor 2018). We derive a higher luminosity and mass-loss rate for MY Cep probably due to the additional contribution from the circumstellar dust with the non-constant mass loss rate.

**Table 5.** Model Results for NGC 7419 Red Supergiants<sup>a</sup>

Star	Sp Type/Temp	Power law( $r^{-n}$ )	$\tau_v$	$r_1$ (AU)	$L_\odot$	$\dot{M}_\odot \text{ yr}^{-1}$
B950(MY Cep)*	M7–7.5 I/3000	1.5	1	73	$3.1 \pm 0.7 \times 10^5$	$2.3 \pm 0.3 \times 10^{-5}$
B435*	M1.5 Iab/3600	2.0	0.05	21	$2.3 \pm 0.5 \times 10^4$	$6.4 \pm 0.9 \times 10^{-8}$
B921*	M0 Iab/3800	...	...	...	$1.4 \pm 0.3 \times 10^4$	no IR excess
B696*	M1.5 Iab/3700	2.0	0.03	27	$3.5 \pm 0.8 \times 10^4$	$4.9 \pm 0.7 \times 10^{-8}$
B139	M1 Iab/3700	2.0	0.03	30	$4.7 \pm 1.0 \times 10^4$	$5.5 \pm 0.8 \times 10^{-8}$

<sup>a</sup>Stars with new FORCAST fluxes have an asterisk.

Beasor & Davies (2016, 2018) argue that a variable dust condensation temperature ( $T_{in}$ ) gives better fits to the SEDs, and suggest that stars with lower  $\dot{M}$  have a larger spread in  $T_{in}$ . The dust formation temperature however depends only on the dust chemistry, vapor pressure, and properties of the grains (Gail et al. 2013) and is independent of the mass-loss rate. The temperature of the inner shell,  $T_{in}$ , however, via  $r_{min}$  will alter the  $\dot{M}$ . Given the lack of a physical mechanism for similar stars to have significantly different dust condensation temperatures, we adopt the same  $T_{in}$  at 1000K for all the stars. A lower  $T_{in}$ , such as 750K, within the expected range for silicate dust, will approximately double the mass loss rate.

#### 4.2. RSGC3

RSGC3, one of the three highly obscured clusters discovered near the base of the Scutum/Crux spiral feature has, on average, the lowest luminosity population of red supergiants among the four clusters discussed in this paper. Only four of its probable members shows evidence for significant circumstellar dust at the long wavelengths. Two independent investigations by Alexander et al. (2009) and by Clark et al. (2009) announced the discovery of this cluster at about the same time. In this paper we use the star numbers from Clark et al. (2009) because they give a longer list of members and candidates.

Clark et al. (2009) list 15 members in their core group based on the photometry plus 7 additional likely members. They also include a third group described as “stars of interest” based on their magnitudes and colors. Alexander et al. (2009) list 8 probable members, 6 candidates and 2 foreground stars. Their 8 members are in the Clark et al. (2009) core group. Only one star, (RSGC3-10) included in the core group by Clark et al. (2009), is considered a candidate by Alexander et al. (2009). In addition to the published 2MASS and Glimpse photometry, both groups also obtained low to moderate resolution near-infrared spectroscopy for spectral classification and for confirmation of the stars’ red supergiant status based on the CO band head absorption.

We measured long wavelength fluxes for 9 members of the core group that were visible in the SOFIA/FORCAST frame. The fluxes for these stars in the Appendix range from 5.5 to 11.1 $\mu$ m. They were not detected at longer wavelengths even though those images were observed. For our analysis with DUSTY, we added 11 stars that are considered members and candidates with mid to far-IR fluxes from other sources.

The greatest uncertainty in our analysis and subsequent discussion of the stars in RSGC3 is the adopted distance and therefore the luminosity of the stars, and their mass-loss rates. Clark et al.

(2009) suggest a distance of  $6 \pm 1$  kpc based on the cluster’s location at the tip of the Galactic bar, similar to RSGC1 and RSGC2, with a possible maximum distance of 7.2 kpc based on the measured interstellar extinction. Alexander et al. (2009) also suggest a distance of 7.2 kpc based on the adopted mean colors and corresponding absolute magnitudes.

As already emphasized above, our adopted distance of  $6 \pm 1$  kpc distance leads to an uncertainty of  $\approx 37\%$  in the derived luminosities. The spectral types in these two papers differ by an average of  $\pm$  one and a half spectral sub-types, or approximately  $\pm 100$  K corresponding to an uncertainty of 10% in the luminosity. Both Clark et al. (2009) and Alexander et al. (2009) estimate a mean  $A_K$  of 1.5 mag corresponding to  $A_V$  of 12.6 to 13.0 mag. Although the two extinction estimates agree, we assume an error of  $\pm 0.1$  mag in  $A_K$ , or 7% on the luminosity, and the residuals of the fit to the SEDs, average 6%. Combining the errors gives an uncertainty of 43% in the luminosity and 28% in the mass loss rate.

Our derived parameters and the results of the DUSTY modeling are summarized in Table 6 for 20 probable and candidate members. Comparison of our luminosities with those for eight stars in common with Clark et al. (2009) agree within the quoted errors in both papers, but we note that our luminosities are systematically lower by 0.12 dex, on average.

**Table 6.** Model Results for RSGC3 Red Supergiants<sup>a</sup>

Star	Sp Type/Temp	Power law( $r^{-n}$ )	$\tau_v$	$r_1$ (AU)	$L_\odot$	$M_\odot \text{ yr}^{-1}$	Comment <sup>b</sup>
RSGC3-1*	... /3600	2.0	0.1	27	$3.7 \pm 1.6 \times 10^4$	$1.7 \pm 0.5 \times 10^{-7}$	A-4, M0
RSGC3-2*	M3 Ia/3800	2.0	0.07	25	$2.9 \pm 1.0 \times 10^4$	$1.1 \pm 0.4 \times 10^{-7}$	A-8, K5
RSGC3-3	M4 Ia/3500	1.5	0.1	37	$7.3 \pm 3.1 \times 10^4$	$2.4 \pm 0.7 \times 10^{-6}$	A-6 M4, ( $2.3 \times 10^{-7}$ )
RSGC3-4*	M3 Ia/3600	1.7	0.1	32	$5.0 \pm 2.1 \times 10^4$	$8.2 \pm 2.3 \times 10^{-7}$	A-7, M2, ( $1.9 \times 10^{-7}$ )
RSGC3-5*	M2 Ia/3800	1.7	0.1	31	$4.7 \pm 2.0 \times 10^4$	$8.1 \pm 0.5 \times 10^{-7}$	A-3, M1
RSGC3-6*	RSG/4000	...	...	...	$2.7 \pm 1.1 \times 10^4$	...	A-1, K5, no IR excess
RSGC3-7*	M0 Ia/3800	2.0	0.2	26	$2.9 \pm 1.2 \times 10^4$	$3.1 \pm 0.9 \times 10^{-7}$	A-5, K4
RSGC3-8	K5 Ia/3800	...	...	...	$1.8 \pm 0.8 \times 10^4$	...	A-12, cand., no IR excess
RSGC3-9	M0 Ia/3800	...	...	...	$2.8 \pm 1.2 \times 10^4$	...	A-9, K4, no IR excess
RSGC3-10*	M0 Ia/3800	...	...	...	$1.0 \pm 0.4 \times 10^4$	...	A-10, cand., no IR excess
RSGC3-11	RSG/4000	...	...	...	$2.7 \pm 1.1 \times 10^4$	...	no IR excess
RSGC3-12	... /4000	2.0	0.1	28	$1.7 \pm 0.7 \times 10^4$	$1.1 \pm 0.3 \times 10^{-7}$	...
RSGC3-13	RSG/3600	1.7	0.1	36	$6.5 \pm 2.8 \times 10^4$	$9.4 \pm 2.6 \times 10^{-7}$	... , ( $2.2 \times 10^{-7}$ )
RSGC3-14	RSG/3300	2.0	0.1	22	$2.4 \pm 1.0 \times 10^4$	$1.3 \pm 0.4 \times 10^{-7}$	A-16, cand.
RSGC3-15	RSG/3200	1.3	0.4	29	$5.0 \pm 2.0 \times 10^4$	$7.9 \pm 2.2 \times 10^{-6}$	
RSGC3-16	RSG/3200	2.0	0.1	30	$4.4 \pm 1.9 \times 10^4$	$1.8 \pm 0.5 \times 10^{-7}$	
RSGC3-17	...	1.5	0.7	...	...	...	see text
RSGC3-21	...	1.5	0.1	...	...	...	see text
RSGC3-27*	...	1.7	0.1	...	...	...	A-13, cand. see text
RSGC3-A-11*	...	1.6	0.1	...	...	...	cand. see text

<sup>a</sup>Stars with FORCAST fluxes have an asterisk.

<sup>b</sup>The Comment includes the designation and spectral type from Alexander et al. (2009) and  $\dot{M}$  for a constant mass loss rate,  $n = 2$ , for those cases where the power law discrimination is less certain.



The most luminous members show evidence in their SEDs for circumstellar dust with silicate emission features, not apparent in the other member stars. RSGC3-15, however, is exceptional with a very strong silicate emission and higher optical depth. Although a spectral type is not available, its relative low temperature of 3200 K is consistent with significant circumstellar dust. Its SED is shown in Figure 6 together with RSGC3-13. The latter’s SED illustrates the uncertainty in adopting the best power law fit and the  $\dot{M}$  especially with the lack of longer wavelength fluxes. For this star and two others, we include the  $\dot{M}$  for constant mass loss in the comment column in Table 6. Five of the members have little or no circumstellar dust like the less luminous RSGs in N7419. For these stars no  $\dot{M}$  is given in the Table.

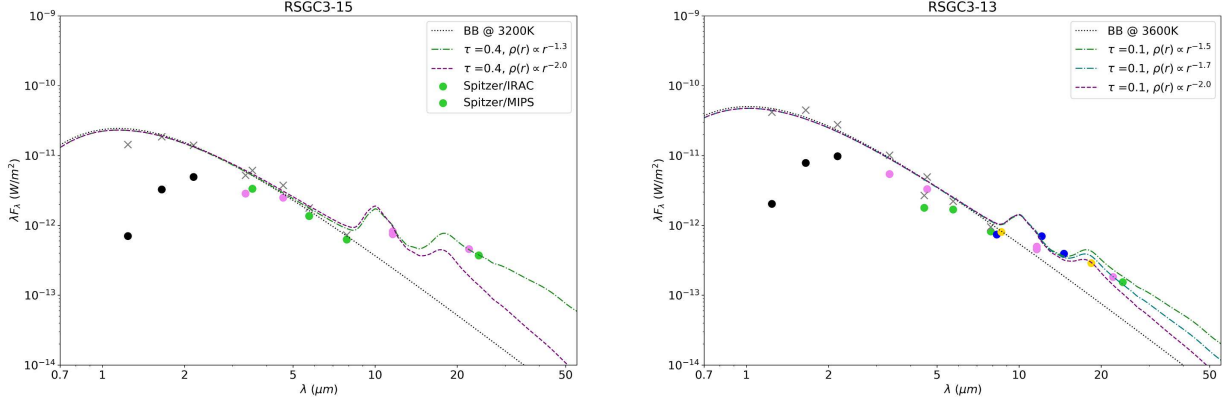


**Figure 6.** Left: The observed and extinction corrected fluxes for RSGC3-15, one of the most luminous members, with very strong silicate emission due to circumstellar dust. The DUSTY fits support a higher  $\tau$ , and a less steep power. Right: The SED for RSGC3-13 is an example of the uncertainty in the power law fits with the DUSTY models. The color-coded symbols are the same as in Figure 5 with the addition of Spitzer/IRAC and MIPS fluxes.

Four of the stars included in Table 6, however are anomalous in the sense that they are much redder than the other members which may be due to higher interstellar extinction, some possible circumstellar reddening, or they may not be members, but background stars. RSGC3-27 (A13) and A11 are both located in the core or central region of the cluster (see Figure 1 in Alexander et al. 2009) and were thus on our SOFIA/FORCAST frame. Both are noteworthy as the reddest stars in the two-color diagram in Alexander et al. (2009) who consider them candidate members. Clark et al. (2009) does not include A11, but considers RSGC3-27 to be a “star of interest”. Their SEDs, corrected for the adopted interstellar extinction, imply temperatures below 3000 K. Thus they likely have higher extinction. Assuming that they are RSGs, and estimating their extinction from the observed colors, the resulting SEDs imply unrealistic high temperatures. We note however that the reddening free parameter  $Q_{IR}$ <sup>1</sup> for RSGC3-27 of 0.1, suggests that it may indeed be an earlier-type star; the  $Q_{IR}$  for A11 of 0.35 is consistent with an RSG. Neither star has a large 10–20  $\mu\text{m}$  silicate emission feature which probably eliminates circumstellar dust as a contributor to the colors.

RSGC3-17 and 21 are similarly very red stars, and are considered likely members by Clark et al. (2009). Like RSGC3-27 and A11, their colors and SEDs suggest that they have higher interstellar extinction. Their  $Q_{IR}$  parameters support their classification as RSGs, but their SEDs corrected for

<sup>1</sup>  $Q_{IR} = (J-H) - 1.8 \times (H-K_s)$  (Clark et al. 2009)

the adopted extinction for RSGC3 imply temperatures even below 2000 K. Given their positions away from the center of the cluster, we suggest that they may both be background stars. RSGC3-17 has a significant silicate emission feature, the largest observed for the RSGC3 stars, and possible additional excess radiation in the 3–8  $\mu\text{m}$  region. Therefore it very likely has some additional circumstellar extinction unlike the other stars in RSGC3, and may not be a member.

The SEDs for RSGC3-17 and A11 are shown in Figure 7. Spectra and radial velocities are needed for these four stars to confirm or not their membership in RSGC3. Due to these uncertainties, they are not included in later discussion.

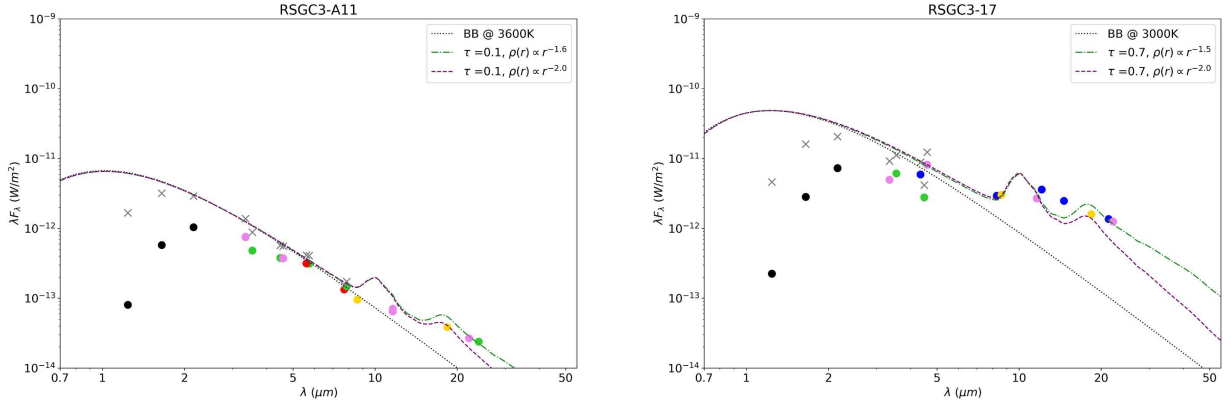


**Figure 7.** The SEDs for RSGC3-A11 (left) and RSGC3-17 (right). Both stars are very red suggesting that they have additional extinction. Planck curves with temperatures consistent with their spectral types do not fit the observed SEDs corrected for the adopted interstellar extinction. A11 would require a temperature below 3000 K and RSGC3-17 below even 2000 K. It has a significant silicate emission feature and possible excess radiation in the mid-infrared quite different from the other RSGC3 red supergiants and may be a background star. See text for more discussion. The symbols are the same as in Figures 5 and 6.

### 4.3. RSGC2

RSGC2 is the second highly reddened cluster with an unprecedented number of red supergiant members and candidates (Davies et al. 2007), and like the other two it is located at the base of the Scutum-Crux spiral arm. It was first noticed by Stephenson (1990) who commented on the number of red stars. Hence it is also known as Stephenson 2. Davies et al. (2007) obtained near-infrared spectra for classification based on the CO bands and radial velocities and compiled the available infrared photometry from 2MASS, Glimpse, and MSX for discussion of their luminosities and the foreground extinction. Based on the spectral types and velocities they identify a core group of 26 probable RSG members. Negueruela et al. (2012, 2013) reported far-red spectra for a subset of the stars with improved spectral types based on atomic-line and molecular-band strengths.

Davies et al. (2007) derive a kinematic distance of  $5.8 \text{ kpc} \pm \approx 1 \text{ kpc}$  and estimate a mean foreground extinction of  $A_K = 1.44 \text{ mag}$  ( $A_V = 12.9 \text{ mag}$ ) from the observed colors of the individual stars. As the authors note, several of the candidate members have much higher extinction and in some cases it may include a contribution from circumstellar dust. We therefore re-measure the mean  $A_K$  deleting several stars, derive a mean of  $1.32 \text{ mag} \pm 0.13 \text{ mag}$  from 18 stars ( $A_V = 11.9 \text{ mag}$ ), and adopt a 10% error on the luminosity from the uncertainty in the foreground extinction. The combined error on the luminosity and mass loss rate for RSGC2 is the same as for RSGC3.

RSGC2 is extended over about  $6'$  and would require two pointings with FORCAST to include the majority of the RSG members. We made a single pointing centered on the highest-density concentration of RSGs around stars 14 and 15. Our FORCAST measurements for the 10 RSGs in the frame are in Table B3. The long wavelength fluxes range from  $7.7$  to  $37.1\mu\text{m}$ . In addition to these 10 stars we added 5 RSG members with mid- to far-infrared fluxes from the other sources for inclusion in our DUSTY modeling and analysis. Our derived parameters and results are summarized in Table 7 for 15 red supergiants. Our luminosities agree quite well for eight stars in common with [Davies et al. \(2007\)](#); well within the quoted errors and with no systematic difference.

**Table 7.** Model Results for RSGC2 Red Supergiants<sup>a</sup>

Star	Sp Type/Temp	Power law( $r^{-n}$ )	$\tau_v$	$r_1$ (AU)	$L_\odot$	$M_\odot \text{ yr}^{-1}$	Comment
RSGC2-2*	M3(M7/3200) <sup>b</sup>	1.5	0.4	52	$1.6 \pm 0.7 \times 10^5$	$1.3 \pm 0.4 \times 10^{-5}$	Stephenson 2
RSGC2-3*	M4(M5/3400)	2.0	0.2	46	$8.8 \pm 3.8 \times 10^4$	$5.1 \pm 1.4 \times 10^{-7}$	Stephenson 10
RSGC2-5	M4(M5/3400)	1.5	0.3	47	$1.0 \pm 0.4 \times 10^5$	$5.8 \pm 1.6 \times 10^{-6}$	...
RSGC2-6*	M5(M3.5/3600)	2.0	0.1	31	$5.3 \pm 2.3 \times 10^4$	$2.0 \pm 0.6 \times 10^{-7}$	Stephenson 1
RSGC2-8*	K5/3900	2.0	0.1	43	$8.4 \pm 3.4 \times 10^4$	$2.6 \pm 0.7 \times 10^{-7}$	Stephenson 4
RSGC2-10*	M5/3500	2.0	0.1	37	$7.2 \pm 3.1 \times 10^4$	$2.2 \pm 0.6 \times 10^{-7}$	...
RSGC2-11*	M4/3600	2.0	0.1	31	$4.9 \pm 2.1 \times 10^4$	$1.9 \pm 0.5 \times 10^{-7}$	...
RSGC2-13	M4/3700	2.0	0.08	30	$4.2 \pm 1.8 \times 10^4$	$1.4 \pm 0.5 \times 10^{-7}$	...
RSGC2-14*	M3/3600	2.0	0.1	23	$2.7 \pm 1.2 \times 10^4$	$1.4 \pm 0.4 \times 10^{-7}$	Stephenson 5
RSGC2-15*	M2/3700	...	...	...	$1.4 \pm 0.6 \times 10^4$	...	Stephenson 6, no IR excess
RSGC2-17	K3/4000	...	...	...	$4.7 \pm 2.0 \times 10^4$	...	no IR excess
RSGC2-18*	M4(M0.5/3800)	...	...	...	$5.3 \pm 2.3 \times 10^4$	...	Stephenson 7, no IR excess
RSGC2-23	M4/3500	2.0	0.1	34	$5.9 \pm 2.5 \times 10^4$	$2.1 \pm 0.9 \times 10^{-7}$	pec. SED <sup>c</sup> , non-member?
RSGC2-49	K4/4000	1.3	5	115	$3.9 \pm 1.7 \times 10^5$	$7.7 \times 10^{-4}$	large IR excess, see text
...	...	2.0	14.5	145	...	$1.3 \times 10^{-4}$	
RSGC2-52*	M0/3800	1.5	0.1	23	$2.4 \pm 1.0 \times 10^4$	$1.4 \pm 0.6 \times 10^{-6}$	pec SED <sup>c</sup>

<sup>a</sup>Stars with FORCAST fluxes have an asterisk.

<sup>b</sup>The improved spectral types from [Negueruela et al. \(2012, 2013\)](#) are given in parenthesis. These types and temperatures are used in our discussion and analysis

<sup>c</sup>Although our Planck curve fits to the SEDs for RSGC3-12 and 52 yielded reasonable results, they failed to fit the J-band fluxes for the expected range of temperatures. [Davies et al. \(2007\)](#) derive somewhat higher  $A_K$  values for these two stars which may be due to circumstellar extinction or variable extinction in the field. Using these higher values, however, as in the case of examples in RSGC3 like A11, gave temperatures inconsistent with the spectral types. We suggest that based on its radial velocity and position, RSGC2-23 may be a background star with higher extinction, but RSGC2-52 is in the core of the cluster. [Negueruela et al. \(2012\)](#) also suggests RSGC2-23 is a non-member.

RSGC2 has a more luminous population of red supergiants and although the range of their luminosities overlap those in RSGC3, this cluster includes at least three stars with luminosities above  $10^5 L_\odot$ , and with corresponding higher mass loss rates including a very late and rare M7, RSGC2-02 and a probable post-red supergiant, RSGC2-49. The SEDs for the majority of the stars also reveal silicate emission at the long wavelengths due to circumstellar dust. The SEDs for two of the most luminous stars are shown in Figure 8.

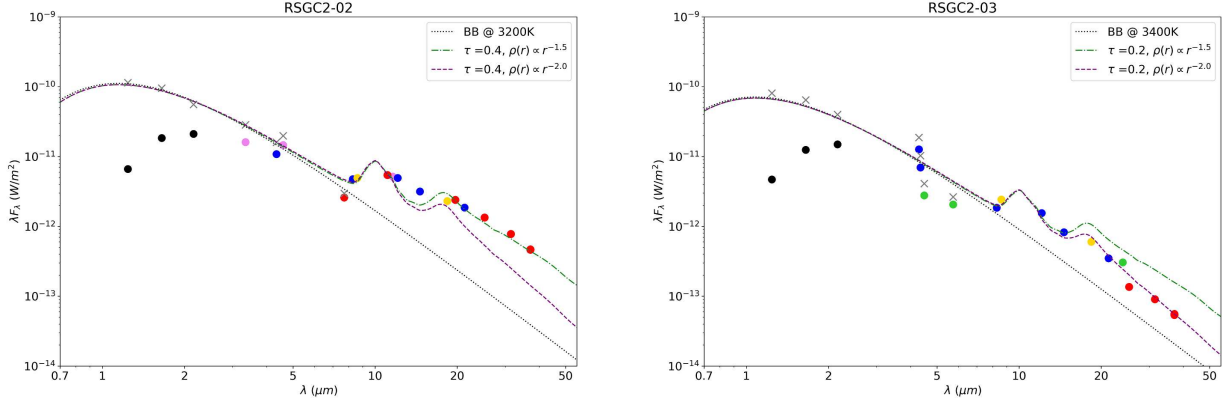


**Figure 8.** RSGC2-02 (left) and RSGC2-03 (right) are two of the most luminous red supergiants in RSGC2, but long wavelength fits from DUSTY yield somewhat different models for their mass loss. RSGC2-02 is the M7 red supergiant which very likely accounts for its strong silicate emission and high mass loss rate. RSGC2-3 is also a late-type M5 and has strong silicate emission but shows a good fit with a constant mass loss rate. These two stars have obviously had different mass loss histories. The symbols are the same as in Figures 5 and 6.

There are a surprisingly large number of very late-type, M4, M5 and an M7, supergiants in RSGC2. This was also noted by [Davies et al. \(2007\)](#). Red supergiants with these late spectral types are relatively rare in the Solar neighborhood ([Humphreys 1979](#); [Elias et al. 1985](#)). The prominence of earlier M spectral types in the Magellanic Clouds, compared to our Solar neighborhood, for example, is attributed to the reduced metallicity and therefore lower opacity in the atmospheres of the RSGs in the Clouds. So perhaps the shift to later types in RSGC2 is due to the expected higher metallicity towards the Galactic center, although the same shift to later M types is not apparent in RSGC3. Red supergiants with these later M types are also associated with enhanced circumstellar dust and high mass loss and thus may be related to the evolutionary state of the stars.

[Negueruela et al. \(2013\)](#) have suggested that RSGC1-01 may be a member. Their spectra show a very late-type RSG similar to RSGC2-02. The star’s radial velocity is slightly offset from the other members by about  $20 \text{ km s}^{-1}$ . It is located away from the central region of the cluster and it is by far the brightest star in the field in the K-band image (see Figures 1 and 4 in [Davies et al. \(2007\)](#)). It is not in the FORCAST FOV, so we determined its SED from published fluxes. Adopting the distance to RSGC2, the mean extinction, and integrating its SED yields  $6.3 \times 10^5 L_{\odot}$  which would make it clearly the most luminous member of the cluster, and much more luminous than RSGC2-02 and the post-RSG star RSGC2-49. But its SED is somewhat peculiar. With the adopted extinction, the 2MASS J and H band fluxes cannot be fit with a range of appropriate temperatures for an RSG. Their fluxes suggest a higher extinction. If so RSGC1-01 would be even more luminous. Although these properties do not rule out membership in the cluster, we consider it doubtful. As emphasized by [Negueruela et al. \(2012\)](#), the region of the RSG clusters is complex, extended spatially across and along the line of sight.

The cluster’s most interesting star is RSGC2-49. Its observed SED (Figure 9) clearly shows the evidence for high circumstellar extinction and high mass loss with significant infrared excess radiation from 8 to  $> 20 \mu\text{m}$ . The lack of a silicate emission feature in the 10–20  $\mu\text{m}$  region indicates that the emission is optically thick. Based on its apparent early K spectral type, luminosity and position in

the HR Diagram (see §5.3), RSGC2-49 is a post-red supergiant similar to IRC +10420 and IRAS 17163-3907 in the Galaxy (Humphreys et al. 1997; Tiffany, et al. 2010; Koumpia et al. 2020) and Var A in M33 (Humphreys et al. 2006).

Star 49’s SED closely resembles that of the famous red supergiant VY CMa (Shenoy et al. 2016) although it is much warmer star. Davies et al. (2007) derived a very high  $A_K$  of 4.6 mag due to a combination of interstellar and circumstellar extinction. Ideally we would correct its SED for the interstellar extinction component and integrate to the longest wavelengths to account for the flux reradiated by the dust and responsible for the additional circumstellar extinction. Unfortunately longer wavelength fluxes from FORCAST or other sources to better model its energy distribution are not available to estimate its total luminosity, unlike for VY CMa. Instead, we integrate a 4000 K Planck curve fit through the K-band flux corrected for the  $A_K$  of  $\approx 4.6$  mag which should approximate its SED when corrected for the flux reradiated by the dust at longer wavelengths. The total luminosity estimated in this way is  $3.9 \times 10^5 L_\odot$ . This may be an under-estimate. It does not include possible excess radiation from warm dust in the 2–8  $\mu\text{m}$  region. This luminosity is slightly higher than that from Davies et al. (2007) based on the absolute K-band magnitude.

Figure 9 shows the results for two DUSTY models relative to its optically-thick silicate emission. Both require high values of  $\tau_v$ , and both yield high values of the mass loss rate, on the order of  $1.3$  to  $7 \times 10^{-4} M_\odot \text{ yr}^{-1}$ . These are not exceptional mass loss rates for hypergiants. Similar rates are measured for stars like IRC +10420, Var A and for red supergiants like VY CMa and NML Cyg. As a probable post-RSG star, we suspect that star 49 is experiencing constant as well as possible variable mass loss in the past as observed for IRC +10420 (Shenoy et al. 2016).

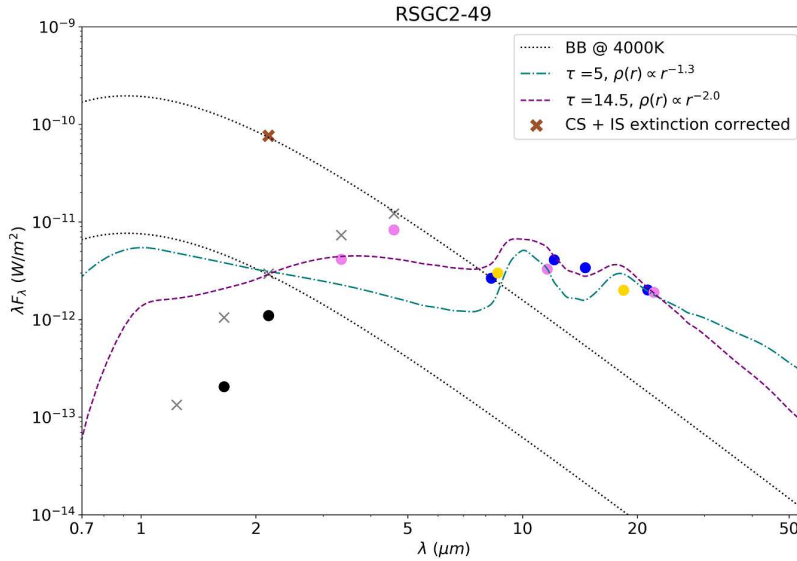


**Figure 9.** The SED for RSGC2-49. Its SED clearly reveals a large infrared excess and the impact of high circumstellar extinction on the observed fluxes. We show the observed fluxes corrected for the mean interstellar extinction adopted for RSGC2 with a 4000K Planck curve fit through the K-band flux. The red tipped cross shows the K band flux corrected for the  $A_K$  extinction from Davies et al. (2007) attributed to both interstellar and circumstellar dust. The silicate emission feature is optically thick; the figure shows the results from two DUSTY models fit through the observed K-band flux corrected for foreground interstellar extinction. See the text for more discussion. The symbols are the same as in the previous SEDs.



#### 4.4. RSGC1

RSGC1 is the youngest of the clusters and its RSG members are the most luminous. Near-infrared spectra in the discovery paper by [Figer et al. \(2006\)](#) and in the follow-up paper ([Davies et al. 2008](#)) provide confirmation of the red supergiant status of 15 stars based on the strength of the CO band heads. All of the members (except star 14) discussed here have luminosities above  $10^5 L_{\odot}$  and with, on average, higher mass loss rates than measured for the red supergiants in the other clusters. RSGC1 is thus critical for establishing the shape of the mass loss rate-luminosity relation for the most luminous RSGs.

Like RSGC2 and RSGC3, RSGC1 is located near the junction of the Scutum-Crux spiral arm and the tip of the Galactic bar. Published distances for RSGC1 range from 5.8 kpc ([Figer et al. 2006](#)) to 6.6 kpc ([Davies et al. 2008](#))  $\pm 0.9$  kpc. It may be the most distant of the four clusters and also suffers from very high and uncertain interstellar extinction. The two references above, respectively estimate  $A_K$  values of 2.74 and 2.60 mag which imply visual extinction as high as 25 to 30 mag. Almost all of these stars show evidence in their SEDs for circumstellar dust and extinction in addition to the interstellar component. To separate the interstellar component, [Beasor et al. \(2020\)](#) select RSGC1-14, the lowest luminosity RSG in the cluster, assume no additional circumstellar extinction, and determine  $A_V$  of  $25 \pm 2$  mag. We adopt  $A_K$  of  $2.29 \pm 0.2$  mag for this same star for the mean interstellar extinction in this paper. Although we suspect that the extinction correction is more uncertain, it contributes a 10% uncertainty to the luminosity as in the other clusters. The difference in the published spectral types from [Figer et al. \(2006\)](#) and from [Davies et al. \(2008\)](#) is  $\pm$  two subtypes, or  $\approx \pm 200$  K. There is more scatter in the fluxes from the different sources for the stars in this cluster which may be due to the faintness of the stars or to variability in these more luminous RSGs. As a result, highly discrepant points were deleted from the fits to the SED and the error from the residuals is larger than in the other clusters and more variable from star to star. An uncertainty of  $\approx 15\%$  on the derived luminosity is typical. The combined error is 47% in luminosity and 28% in the mass loss rate.

The SEDs of all of the stars observed with FORCAST show significant silicate emission features and extended emission longward of  $20 \mu\text{m}$  (except the yellow hypergiant RSGC1-15). Figure 10 shows the SEDs for two of the members. The results of our DUSTY modeling are summarized in Table 8. The spectral types from the strength of the CO bands from [Figer et al. \(2006\)](#) and from [Davies et al. \(2008\)](#) are both listed, in that order, with our adopted temperature for the SED fits.

Maser emission is measured in four of the most luminous red supergiants; RSGC1-01, 02, and 04 show SiO emission while RSGC1-13 is the source of SiO, H<sub>2</sub>O and OH emission. All four are quite dusty and have relatively high mass loss rates. The SED for RSGC1-13 in Figure 11 illustrates its strong silicate emission and very dusty excess emission out to  $40 \mu\text{m}$ . Given its multiple maser emissions and earlier K spectral type, RSGC1-13 is probably the most evolved RSG and has already begun its transition back to warmer temperatures. This possibility is supported by the presence of RSGC1-15, a probable yellow hypergiant member of the cluster. RSGC1-13 has the highest measured  $\dot{M}$  in RSGC1, however it does not share the very high circumstellar extinction visible in the SED for RSGC2-49. This suggests that it has not yet experienced the high mass loss episodes visible in the ejecta and SEDs of many post-RSG hypergiants.

Unfortunately, insufficient data is available for the yellow hypergiant RSGC1-15 at wavelengths beyond  $7 \mu\text{m}$  to model its circumstellar dust and  $\dot{M}$ . In addition to 2MASS data, published fluxes



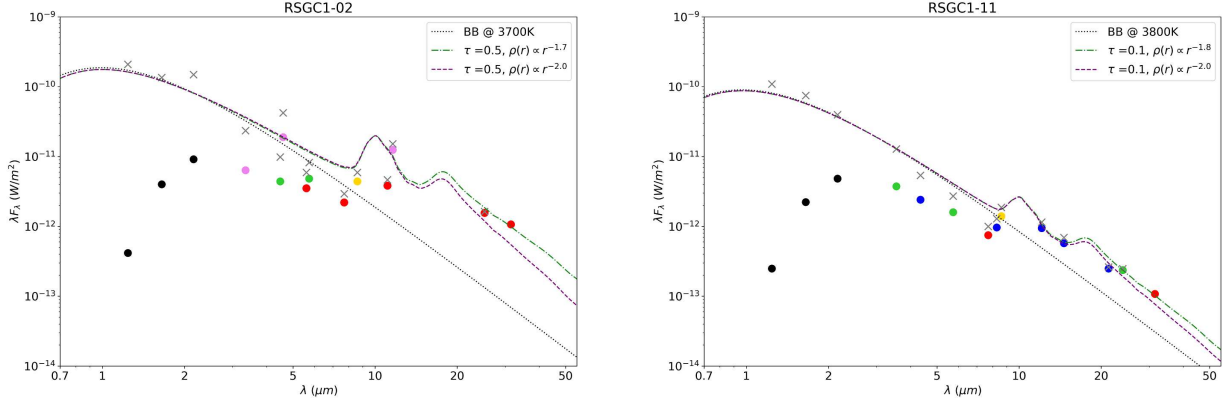


**Figure 10.** Left: RSGC1-02 is one of the most luminous members with SiO maser emission and a prominent silicate emission feature with a corresponding high mass loss rate. Right: RSGC1-11 has a comparable luminosity and while it also has silicate emission, it is weaker with a lower mass loss rate. The SEDs for both stars illustrate the scatter in the observed fluxes from different sources for the stars in this cluster. In our adopted fits from DUSTY we emphasize the longest wavelength measurements from SOFIA/FORCAST and Spitzer. The symbols are the same for the other SEDs.

**Table 8.** Model Results for RSGC1 Red Supergiants<sup>a</sup>

Star	Sp Type/Temp	Power law( $r^{-n}$ )	$\tau_v$	$r_1$ (AU)	$L_\odot$	$M_\odot \text{ yr}^{-1}$	Comment
RSGC1-01*	M3/M5/3550	1.6	0.5	83	$3.35 \pm 1.6 \times 10^5$	$1.7 \pm 0.5 \times 10^{-5}$	SiO maser
RSGC1-02*	M4/M2/3700	1.7	0.5	69	$2.15 \pm 1.0 \times 10^5$	$9.0 \pm 2.5 \times 10^{-6}$	SiO maser
RSGC1-03*	M4/M5/3500	1.5	0.5	48	$1.2 \pm 0.5 \times 10^5$	$1.5 \pm 0.4 \times 10^{-5}$	...
RSGC1-04*	M0/M1/3800	1.7	0.4	93	$3.8 \pm 1.8 \times 10^5$	$9.7 \pm 2.8 \times 10^{-6}$	SiO maser
RSGC1-05*	M6/M4/3500	1.3	0.1	61	$1.9 \pm 0.9 \times 10^5$	$8.2 \pm 2.3 \times 10^{-6}$	...
RSGC1-06*	M5/3400	1.9	0.5	68	$2.3 \pm 1.1 \times 10^5$	$3.4 \pm 1.0 \times 10^{-6}$	...
RSGC1-07*	M2/M3/3800	1.7	0.2	65	$1.9 \pm 0.9 \times 10^5$	$3.4 \pm 0.9 \times 10^{-6}$	...
RSGC1-08*	M3/M3/3600	1.6	0.1	63	$2.0 \pm 0.9 \times 10^5$	$2.6 \pm 0.7 \times 10^{-6}$	...
RSGC1-09*	M3/M6/3600	1.5	0.1	54	$1.5 \pm 0.7 \times 10^5$	$3.5 \pm 1.0 \times 10^{-6}$	...
RSGC1-10*	M5/M3/3600	1.5	0.1	68	$2.35 \pm 1.1 \times 10^5$	$4.4 \pm 1.2 \times 10^{-6}$	...
RSGC1-11*	M1/M4/3800	1.8	0.1	65	$2.0 \pm 0.9 \times 10^5$	$1.7 \pm 0.5 \times 10^{-6}$	...
RSGC1-12*	M0/3900	2.0	0.1	64	$1.9 \pm 0.9 \times 10^5$	$3.4 \pm 1.0 \times 10^{-7}$	...
RSGC1-13*	M3/K2/4200	1.7	0.5	85	$2.9 \pm 1.4 \times 10^5$	$2.7 \pm 0.8 \times 10^{-5}$	SiO, H <sub>2</sub> O, OH maser
RSGC1-14	M3/M1/3700	2	0.05	39	$7.4 \pm 3.5 \times 10^4$	$1.9 \pm 0.5 \times 10^{-7}$	...
RSGC1-15*	G0/G6/ ...	...	...	...	$6.2 \pm 2.9 \times 10^5$ : ...	post RSG, see text	...

<sup>a</sup>Stars with FORCAST fluxes have an asterisk.

from Spitzer/IRAC and two data points from the FORCAST images are available, but RSGC1-15 was not detected in the FORCAST images at 11  $\mu\text{m}$  and longer. The published spectral types (Figer et al. 2006; Davies et al. 2008) indicate a range from G0 to G6 based on the strength of the CO band heads, and spectra separated by only four months shows variable emission in the CO band heads (Davies et al. 2008). We get a temperature of  $\approx 8000$  K from the 2MASS fluxes alone and a corresponding luminosity of  $6.2 \times 10^5 L_\odot$  compared to 6900 K and  $2.3 \times 10^5 L_\odot$  from Davies et al.

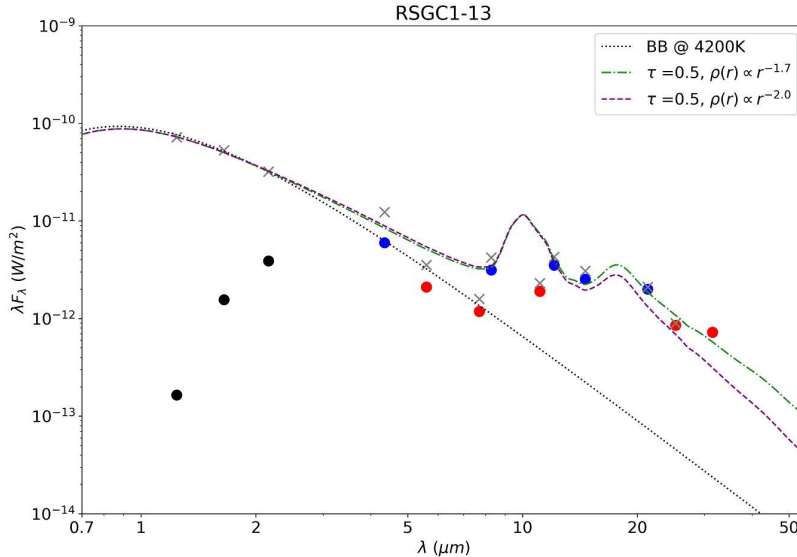


**Figure 11.** The SED for the maser source RSGC1-13. Symbols are the same as in the other SEDs.

(2008). This range in apparent temperature is not surprising for the hypergiants which often have optically-thick winds. RSGC1-15’s variability, possible temperature range, and lack of measurable circumstellar dust is similar to the hypergiant  $\rho$  Cas (Shenoy et al. 2016).

We have eight stars in common with the data for the RSGC1 red supergiants in Beasor et al. (2020). Comparison shows similar derived luminosities well within the quoted errors in both studies, but our mass loss rates estimated from the DUSTY model fits are significantly higher. Beasor et al. (2020) assume a constant mass loss rate in their DUSTY models but in this paper we have allowed the power law to vary. As we show for the RSGC1 supergiants as well as for red supergiants in the other clusters, a variable mass loss rate often yields a better representation of the long wavelength fluxes. This alternative result will affect the mass-loss rate-luminosity relation for the red supergiants discussed in the next section.

## 5. RESULTS AND DISCUSSION

### 5.1. The Mass-Loss Rate – Luminosity Relation for Red Supergiants

The empirical  $\dot{M}$  - Luminosity relation for red supergiants is critical to the models and evolutionary tracks for evolved stars. Not only does it allow the calculation of the total mass lost during this end stage for many stars, but whether the rate has been constant or episodic may determine whether the star will evolve on a blue loop back to warmer temperatures before the terminal state. This latter possibility is now important with respect to the progenitors of supernovae and possible alternative final stages for massive stars.

Several  $\dot{M}$  - L relations are available in the literature; including for example, Reimers (1975), Van Loon et al. (2005) and by de Jager and collaborators (de Jager et al. 1988; Nieuwenhuijzen & de Jager 1990). The de Jager prescriptions are the most commonly used in the evolutionary models. There are not only differences in the predictions among these relations, but also significant scatter within each. This latter should not be surprising though since it is reasonable to expect the stars to continue to evolve during the RSG stage with  $\dot{M}$  increasing with time, the  $\dot{M}$  may be variable, and they may experience high mass loss episodes as observed in some of the most evolved red supergiants.

Mauron & Josselin (2011) have published a thorough review of the different published relations and conclude that the de Jager prescriptions provide good representations of the expected mass loss rates for the Galactic RSGs with Solar metallicity.

Use of clusters with numerous RSGs may reduce some of the observed internal scatter in the relation by removing some of the uncertainty due different distances and ages. In a series of papers Beasor & Davies (2016, 2018); Beasor et al. (2020) have examined the  $\dot{M}$  - L relation for several clusters; NGC 7419,  $\chi$  Per, NGC 2100 in the LMC, and RSGC1. RSGs with luminosities generally below  $10^5 L_\odot$  are represented by the stars in NGC 7419,  $\chi$  Per, and NGC 2100, while the more luminous RSGs ( $\geq 10^5 L_\odot$ ) are in RSGC1. The first group of clusters yields a  $\dot{M}$  - L relation that is much steeper than all of the previous prescriptions with several of the lower luminosity RSGs significantly below the de Jager et al. (1988) and Nieuwenhuijzen & de Jager (1990) relations. The more luminous RSGs in RSGC1 however lie on a distribution that is curiously offset from and even below that for the less luminous supergiants (see Figure 2 in Beasor et al. 2020). The authors argue that this is an initial mass effect such that the more massive stars have a lower mass loss rate for a given luminosity.

In this paper, we have treated the DUSTY models somewhat differently by allowing the mass loss rate to vary. Our data include stars in NGC 7419 and RSGC1 in common with Beasor and Davies plus RSGC2 and RSGC3 with many stars in the  $10^4 - 10^5 L_\odot$  range.

Our  $\dot{M}$  - L relation for the four clusters is shown in three panels in Figure 12. The top panel (A) simply shows our data with the average error in the logs for each cluster. In the middle panel (B) we've added the two linear relations from Beasor et al. (2020) for comparison and the bottom panel (C) is our data with the de Jager prescriptions. In Figure 12C, we've added some high luminosity, high  $\dot{M}$  evolved supergiants in the Solar neighborhood for comparison with the position of RSGC2-49, and also to illustrate these extreme stars not represented by the general prescriptions. The mass loss rates for these stars are from our two previous papers using SOFIA/FORCAST data with DUSTY models. We adopt the same mass loss equation (A8) with a gas to dust ratio of 200 used for the RSG clusters in this paper for comparison.

At luminosities below  $\approx 10^5 L_\odot$  our data show a significant population of RSGs with mass-loss rates that also lie below the de Jager et al. relations plus a few stars closer to the de Jager curve. These latter stars in RSGC3 and RSGC2 have SEDS that show the presence of circumstellar dust and most are fit with a steady constant mass loss rate. We do not, however, confirm the steep slope for the lower luminosity RSGs reported by Beasor & Davies (2018); Beasor et al. (2020). We note that their steep linear relation is heavily weighted by stars in NGC 2100 in the LMC with a gas/dust ratio of 500. A lower ratio would reduce their  $\dot{M}$  and yield a flatter relation. A higher  $v_{exp}$  for the cluster RSGs would yield a higher  $\dot{M}$ . Velocities of 35- 40 km s<sup>-1</sup> are measured for some high luminosity RSGs, but these are all  $\dot{M}$  stars with complex circumstellar ejecta. We doubt that a higher  $v_{exp}$  is applicable for these lower luminosity RSGs many of which have virtually zero mass-loss rates. Likewise, a higher gas to dust ratio will not move them substantially closer to the de Jager curve.

Our results could be described as representing a lower bound to the mass loss rates for these less luminous RSGs. In their review, Mauron & Josselin (2011) also find several RSGS in the Solar region with luminosities between  $\log L_\odot$  of 4.5 to 5.0 that lie below the deJager curve. Although their data do not extend below  $\log L_\odot$  of 4.5, the distribution of their stars are consistent with the less luminous RSGs in Figure 12A.

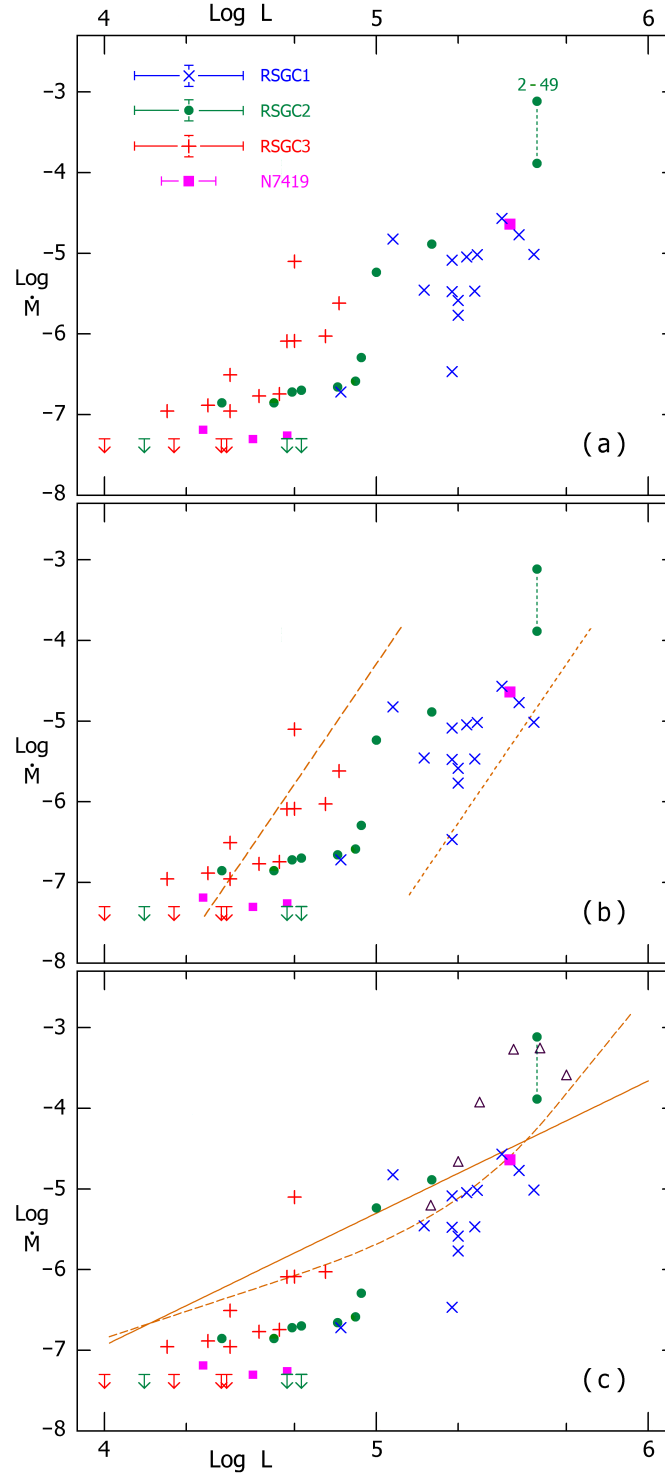


**Figure 12.** Top(12A): The  $\dot{M}$  - Luminosity relation for the RSGs in the four clusters. The color-coded identification for the different clusters is given with the errors in the logs. Those few stars with no infrared excess and no measurable mass loss rates are indicated by downward errors. Middle(12B):  $\dot{M}$  - Luminosity relation for the RSGs in the four clusters with the linear relations from Beasor et al. (2020) shown as dashed lines in red. Bottom(12C):  $\dot{M}$  - Luminosity relation for the RSGs in the four clusters with the prescriptions from de Jager et al. (1988) and Nieuwenhuijzen & de Jager (1990) for  $T_{eff}$  3750K. Several high luminosity, high  $\dot{M}$  are also shown as open triangles. Moving from left to right, with increasing luminosity, the plotted stars are  $\mu$  Cep, S Per, VX Sgr, NML Cyg, VY CMa, IRC 10420. Note the position of  $\mu$  Cep often considered to have an anomalously low  $\dot{M}$ , but with a gas to dust ratio of 200 it falls with the RSGC1 stars.

At luminosities above  $10^5 L_\odot$  there is a rapid transition to higher mass loss rates. Most of the stars, in RSGC1, are close to or just below the de Jager et al. prescriptions in Figure 12C. This is in contrast to the much lower linear relation for the RSGC1 stars in Beasor et al. (2020). These differences are obviously due to the treatment of results from the DUSTY models with a variable power law for the density distribution. If we had used a slightly higher  $v_{exp}$  (35–40 km s<sup>-1</sup>), their  $\dot{M}$  would move them closer to the de Jager relation as would a lower  $T_{in}$ . Thus the distribution of the more luminous RSGs in our study is a reasonable approximation to the prescriptions determined empirically for RSGs in the Solar neighborhood. For example, the  $\dot{M}$ – $L_\odot$  relation in Mauron & Josselin (2011) likewise shows the same shift to significantly higher mass loss rates for stars above  $10^5 L_\odot$  in their study of 39 RSGs in the Solar neighborhood with an independent mass loss rate determination.

The majority of stars used by de Jager et al. (1988) in the Solar region are known semi-regular (SR) variables. The high  $\dot{M}$  stars in Figure 12C are all known variables. The role of variability on the mass loss rates and mass loss histories of the RSGs and other massive stars has been not fully explored. It seems reasonable to us that as stars evolve during the red supergiant stage, their expanded envelope becomes more subject to instabilities that thus enhance their mass loss rate.

Most stellar models and evolutionary tracks have relied on the de Jager et al.  $\dot{M}$  - Luminosity relations for the red supergiants. Our results for the RSGs below  $\approx 10^5 L_\odot$  suggests that a lower  $\dot{M}$  should be adopted as an alternative or better, a possible range of mass loss rates for the less luminous RSGs. Instead of a single linear or curved relation, the  $\dot{M}$  - Luminosity relation may be better represented by a broad band, approximately parallel to the de Jager curve, with a lower bound defined by the low luminosity RSGs in RSGC3 and RSGC2 which at  $10^5 L_\odot$  curves more rapidly upward. This is speculative, but the transition to much higher  $\dot{M}$  at about  $10^5 L_\odot$  corresponds approximately to an initial mass of 18–20  $M_\odot$  which is interestingly close to the upper limit for RSGs becoming Type II SNe.

### 5.2. Evolution in the Red Supergiant Stage

The large number of red supergiants in these four clusters provide a sample with the expected range in RSG luminosities and initial masses from  $\approx 9$  to  $\geq 25 M_\odot$ . They also include examples of more evolved RSGs, such as MY Cep and RSGC2-02, several sources of maser emission, and candidates for post-red supergiant evolution well-represented by RSGC2-49.

Several questions about red supergiant evolution concern their eventual fate as the progenitors of Type II-P supernovae, or possible evolution back to warmer temperatures and their eventual demise as alternative supernovae or in a direct collapse to a black hole. These alternate possibilities very likely depend on their mass loss histories. In the previous section, we showed a complex dependence of  $\dot{M}$  on luminosity with a strong shift to higher mass loss rates as the luminosities of the stars increase above  $10^5 L_\odot$ .

Another question concerns how the stars evolve during the red supergiant stage. Do they slowly ascend the RSG region much like red giants getting more luminous at essentially the same temperature as suggested by Davies et al. (2013), or do they evolve through the RSG stage slowly getting cooler with later spectral types and increased  $\dot{M}$ ? The former is based on a near-constant temperature for RSGs where the TiO based spectral type is a luminosity indicator. The latter model does not rule out some increase in luminosity as the envelope expands and cools.

The HR Diagrams for the four clusters are shown separately in Figure 13 using the luminosities and temperatures in Tables 5 – 8.

**Table 9.** Luminosity–Temperature Dependence

Cluster	N(RSGs)	Temp Range (K)	Lum Range ( $L_{\odot}$ )	Mean Lum ( $L_{\odot}$ )
Binned by Temperature				
RSGC3	9	3800–4000	$1.1\text{--}4.7 \times 10^4$	$2.6 \pm 0.3 \times 10^4$
	4	3500–3600	$3.7\text{--}7.3 \times 10^4$	$5.6 \pm 0.7 \times 10^4$
	3	3200–3300	$2.4\text{--}5.0 \times 10^4$	$3.9 \pm 0.6 \times 10^4$
RSGC2	5	3700–4000	$1.4\text{--}8.4 \times 10^4$	$4.8 \pm 1.0 \times 10^4$
	6	3400–3600	$2.7\text{--}10 \times 10^4$	$6.5 \pm 1.0 \times 10^4$
	1	3200	$1.6 \times 10^5$	...
RSGC1	6	3700–3900	$0.7\text{--}3.8 \times 10^5$	$2.1 \pm 0.9 \times 10^5$
	6	3400–3600	$1.2\text{--}3.4 \times 10^5$	$2.0 \pm 0.7 \times 10^5$
Cluster	N(RSGs)	Lum Range ( $L_{\odot}$ )	Temp Range (K)	Mean Temp (K)
Binned by Luminosity				
RSGC3	12	$10^4\text{--} < 5 \times 10^4$	4000–3200	$3740 \pm 70$
	4	$5 \times 10^4\text{--} < 10^5$	3600–3200	$3675 \pm 80$
	...	...	...	...
RSGC2	5	$10^4\text{--} < 5 \times 10^4$	4000–3600	$3720 \pm 65$
	5	$5 \times 10^4\text{--} < 10^5$	3900–3400	$3640 \pm 80$
	2	$10^5\text{--} 5 \times 10^5$	3400–3200	3300
RSGC1	1	$5 \times 10^4\text{--} < 10^5$	3700	...
	12	$10^5\text{--} 5 \times 10^5$	3900–3400	$3650 \pm 40$

To examine evolution in the red supergiant stage, we first look at the luminosity dependence on the apparent temperature of the stars in each cluster, and as a second test, we examine the temperature in different luminosity ranges. Since there is more than one published spectral type for most stars, even when the authors use the same data, as in RSGC1, we adopt the temperature from our SED fits. This is not strictly a test of the Davies et al hypothesis in which the RSGs all have essentially the same temperature. The results are shown in Table 9 binned by temperature and by luminosity for the three RSG clusters. With only four stars, all about the same temperature and luminosity, N7419 is not included, and in the subsequent discussion we show that MY Cep has very likely evolved from a more massive star.

The results for RSGC1 and RSGC3, binned by temperature, do not support a luminosity dependence on the apparent surface temperature. The luminosity ranges for the different temperature bins overlap. The luminosity distribution of the stars in RSGC2 show some dependence on temperature but the signature is not strong and not statistically significant. The second test, binned by luminosity, supports this conclusion. The range of temperatures in each luminosity range is essentially the same. The highest luminosity range for RSGC2, with only two stars and lower temperatures, supports evolution in the RSG stage to cooler, later types since these are the most luminous, and presumably most massive, evolved members. We conclude that there is no strong evidence that red supergiants evolve significantly up the RSG branch.



The HRDS for the four clusters clearly illustrate the wide range in luminosities, initial masses, and ages of the stars that define the RSG range in the HR Diagram. Evolutionary tracks from Ekstrom et al. (2012), without rotation, are shown on each HRD with initial masses selected to correspond to the range of luminosities of the red supergiants in each cluster. Since NGC 7419 has a large number of Be star members which are rapid rotators, we also show the corresponding tracks with rotation for comparison. In the following discussion, we also compare the HRDs with the isochrones from Ekstrom et al. (2012).

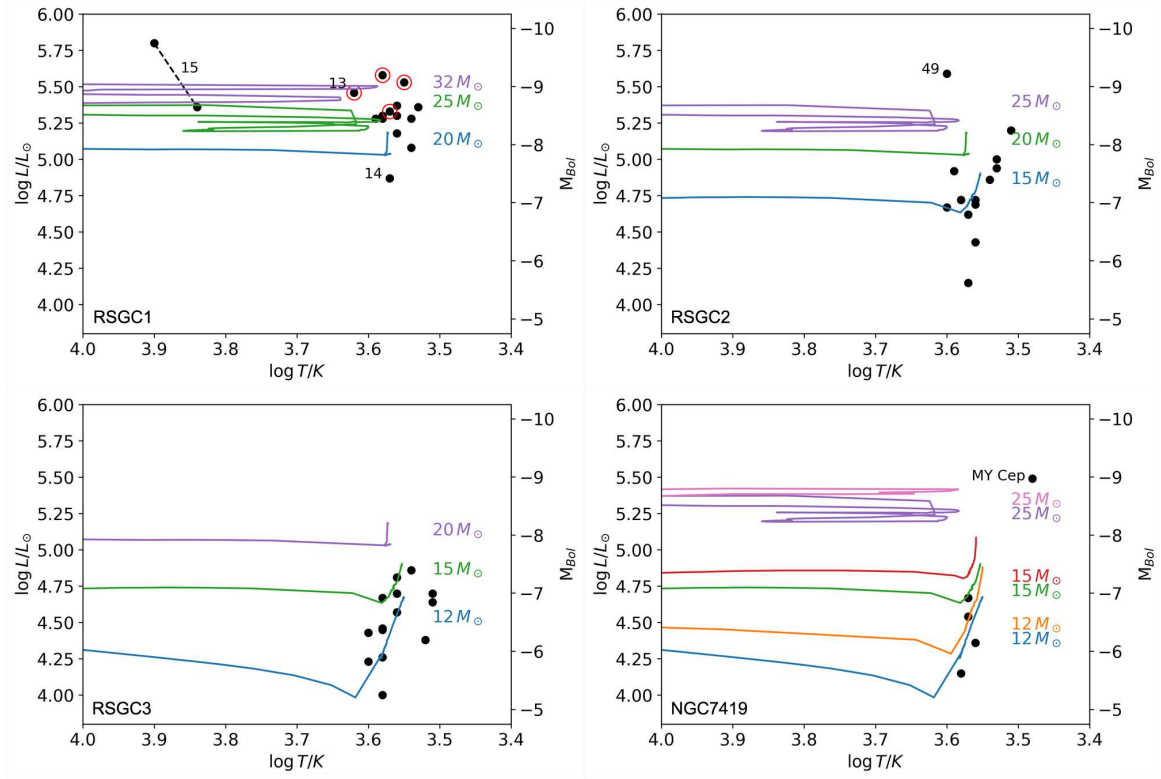


**Figure 13.** The HR Diagrams for the four clusters with the evolutionary tracks from Ekstrom et al. (2012) without rotation. The upper curve in the pairs in the HRD for NGC 7419 is the corresponding model with rotation.

The red supergiants in RSGC1 are mostly clumped in a relatively small luminosity range from  $\approx 10^5$  to  $5 \times 10^5 L_\odot$  implying an initial mass range of 20 to 30  $M_\odot$ . The post-RSG candidate, star 15, may have arisen from a higher mass star but the models for the higher mass ranges show multiple transits across the HRD. We also can't rule out the possibility that the three most luminous members have been on a post-RSG transit. As already mentioned, star 13 is candidate for beginning its evolution back to higher temperatures. Except for star 14, the red supergiants in RSGC1 are consistent with an age no more than 8 Myr. Star 14 is the star discussed earlier with little or no circumstellar dust selected by Beasor et al. (2020) to estimate the foreground extinction. We likewise adopted its extinction. We note that its SED, lack of dust, and very low  $\dot{M}$  are quite different from the other members. It is also located more than  $2'$  from the center of the cluster. We therefore suggest that it may not be a member.

The red supergiant members of RSGC3 show a wide range in luminosities from  $10^4$  to almost  $10^5$  indicating a range in initial masses from  $\approx 9$  to somewhat above  $15 M_{\odot}$ . Despite this wide range in luminosities and initial masses, the isochrones show that the position of these RSGs on the HRD are consistent with a common age of  $\approx 16$  Myr. The lower luminosity stars may have recently entered the RSG stage while the most luminous with initial masses of  $\sim 15 M_{\odot}$  are nearing the end of their red supergiant lives.

RSGC2 and NGC 7419 are the exceptions to a common age for the apparent member red supergiants. RSGC2 has a large range of luminosities overlapping with both RSGC3 and RSGC1, and implying an initial mass range from  $12 M_{\odot}$  to more than  $25 M_{\odot}$  for the post-RSG star 49. As already noted in our previous discussion, the candidate members are spread over more than  $6'$ . This is also a very complex region. [Negueruela et al. \(2012\)](#) emphasized the extent of this region and concluded that RSGC2 is not an isolated cluster but part of a region with numerous massive stars. We therefore suggest that RSGC2 and the surrounding red supergiants is more like a stellar association with populations of massive stars not all the same age. The stars may range in age from 16 Myr to less than 8 Myr.

Comparison of the isochrones with the evolutionary tracks for NGC 7419 suggests that the four lower luminosity red supergiants have essentially the same age, between 16 and 20 Myr with a relatively small range in initial mass from 10 to  $15 M_{\odot}$ . NGC 7419 has a significant population of normal B-type stars as well as Be stars. [Negueruela et al. \(2013\)](#) noted that the most luminous B stars, on the main sequence have  $M_V$ 's of  $\approx -5$  mag. Assuming their early B2 spectral types, their bolometric luminosities would be  $-6.2$  with corresponding initial masses of about  $12 M_{\odot}$ . They and their immediate slightly more massive counterparts are the likely progenitors of the four red supergiants.

MY Cep however is not consistent with their inferred age and initial masses. There is a large gap in luminosity between MY Cep and the four fainter RSGs. MY Cep is easily 6 to 10 times more luminous. Thus it is most likely evolved from a somewhat more massive star. If we assume that it began as a  $20 M_{\odot}$  star, based on the models it would be at most  $\approx 9$  Myr old. The models for even more massive stars show multiple transits across the HRD, but they have similar maximum ages at the end of the tracks. Our previous discussion cast doubt on significant evolution up the RSG branch accompanied by a large increase in luminosity. But, if so, one would then have to ask where are the missing red supergiants that should be found on the HRD between MY Cep and the four fainter stars. An alternative explanation is that MY Cep is not a member. NGC 7419 is in the Perseus spiral arm and in its direction there are a several large associations with mixed populations of massive and evolved stars.

## 6. FINAL REMARKS AND RECOMMENDATIONS

The numerous red supergiants in these four clusters have provided us with a large sample covering the expected initial masses and luminosities for the RSGs. Thus in this paper we have covered a wide range of topics from their SEDs, mass loss rates, the HRDs and their evolutionary state. We conclude that there is no strong statistical support for evolution up the RSG branch, but instead we support evolution during the RSG stage to lower temperatures as their outer envelopes expand with increased mass loss.

Our fits to the SEDs with the DUSTY models allow for a variable power law for the density distribution function and our estimate of the mass loss rates. Our  $\dot{M}$  – Luminosity relation (Figure

12) for 42 RSGs in the clusters follows the [de Jager et al. \(1988\)](#) relation but at luminosities below  $10^5 L_\odot$ , we find a population of RSGs with significantly lower  $\dot{M}$ . At higher luminosities, there is a rapid transition to higher mass loss rates. We note that [Mauron & Josselin \(2011\)](#) show a similar distribution of RSGS in the  $\dot{M} - L$  plane for 39 red supergiants in the Solar neighborhood based on an independent  $\dot{M}$  from the flux at  $60\mu\text{m}$ . Based on our results, we recommend that a lower mass loss rate be adopted, on average, for RSGs below  $10^5 L_\odot$ . Instead of a single linear or curved relation, we suggest that a curved band, parallel to the de Jager relation, is a better representation of the empirical relation with a lower boundary represented by the less luminous RSGs which then curves upward at  $10^5 L_\odot$ . For application to stellar models, the adopted  $\dot{M}$  corresponding to the luminosity could slowly increase as the star evolves during the RSG phase.

We thank Kris Davidson for useful comments and critical reading of the paper. We also thank the LBTI team for making the LMIRCam available for our project and for their support with planning and executing the observations, and the SOFIA Science and Mission Operations team for observation planning and the data reduction. This work was supported by NASA through award SOF 06-0089 to R. M. Humphreys issued by USRA.

*Facilities:* SOFIA(FORCAST), LBT/LBTI(LMIRCam)

## APPENDIX

### A. THE MASS-LOSS RATE FROM DUSTY

DUSTY calculates the optical depth through a model dust shell down to the star using the column number density of dust grains that follow a particular grain size distribution. This size distribution,  $n(a)$ , is defined such that  $n(a)da$  is the number of dust grains per  $\text{cm}^2$  within the size interval  $da$  along the line of sight. Using Mie theory, we can define the effective extinction efficiency  $Q_{\text{eff}}$  at some wavelength as

$$Q_{\text{eff}} = \frac{\int_{a_{\text{min}}}^{a_{\text{max}}} Q(a)n(a)\pi a^2 da}{\int_{a_{\text{min}}}^{a_{\text{max}}} n(a)\pi a^2 da} \quad (\text{A1})$$

The optical depth can be expressed as

$$\tau = Q_{\text{eff}} \int_{a_{\text{min}}}^{a_{\text{max}}} n(a)\pi a^2 da \quad (\text{A2})$$

Using a dust grain mass density  $\rho_d$ , the mass column depth corresponding to the optical depth is

$$m (\text{gm cm}^{-2}) = \int_{a_{\text{min}}}^{a_{\text{max}}} \rho_d n(a) \frac{4}{3} \pi a^3 da \quad (\text{A3})$$

Using an MRN grain size distribution ( $n_0$  in  $\text{cm}^{-3}$ )

$$n(a) = n_0 \left( \frac{a_0}{a} \right)^{3.5} \quad (\text{A4})$$

and after some algebra we have

$$m = \sqrt{a_{\max} a_{\min}} \frac{4 \rho_d \tau}{3 Q_{\text{eff}}} \quad (\text{A5})$$

Although DUSTY softens the dust grain size distribution at  $a_{\max}$ , this has only a minor effect on our simplified formula. DUSTY uses a radial density distribution that follows a power law with index  $n$ . Using this formulation we have

$$\begin{aligned} \rho(r) &= \rho_{r_{\min}} \left( \frac{r_{\min}}{r} \right)^n \\ m &= \int_{r_{\min}}^{r_{\max}} \rho(r) dr \sim \frac{\rho_{r_{\min}} r_{\min}}{n-1} \quad \text{for } n > 1 \text{ and } r_{\max} \gg r_{\min} \end{aligned} \quad (\text{A6})$$

Equating the column mass in eqs. 5 and 6 and solving for  $\rho_{\min}$ , we have

$$\rho_{r_{\min}} = \frac{m(n-1)}{r_{\min}} = \frac{\sqrt{a_{\max} a_{\min}} 4 \rho_d (n-1) \tau}{r_{\min} 3 Q_{\text{eff}}} \quad (\text{A7})$$

Following Shenoy et al. (2016) we can compute the average mass-loss rate over the lifetime for the model shell by assuming a constant wind velocity  $V$  and integrating the density from  $r_{\min}$  to  $r_{\max}$  as follows

$$\begin{aligned} M_{\text{tot}} &= \int_{r_{\min}}^{r_{\max}} 4\pi r^2 \rho(r) dr = \frac{4\pi \rho_{r_{\min}}}{3-n} (r_{\max}^{3-n} r_{\min}^n - r_{\min}^3) \\ \dot{M} &= \frac{M_{\text{tot}} V}{r_{\max} - r_{\min}} \sim \frac{16\pi}{3} \frac{n-1}{3-n} \sqrt{a_{\max} a_{\min}} \rho_d \frac{\tau}{Q_{\text{eff}}} r_{\max}^{2-n} r_{\min}^{n-1} v_{\text{exp}} \end{aligned} \quad (\text{A8})$$

where we assume  $r_{\max} \gg r_{\min}$ . For the case where the index  $n = 2$ , a constant mass-loss rate, we have

$$\dot{M} \sim \frac{16\pi}{3} \sqrt{a_{\max} a_{\min}} \rho_d \frac{\tau}{Q_{\text{eff}}} r_{\min} v_{\text{exp}} \quad (\text{A9})$$

DUSTY outputs the optical depth for the model dust shell at a wavelength of  $0.55 \mu\text{m}$ , so  $Q_{\text{eff}}$  is calculated at this wavelength using the optical constants for cool O-rich silicates from (Ossenkopf et al. 1992). Using optical constants  $n = 2.1$ ,  $k = 0.089$  and a range in grain size  $a_{\min} = 0.005 \mu\text{m}$ ,  $a_{\max} = 0.25 \mu\text{m}$  we compute  $Q_{\text{eff}} = 0.38$  at  $V$ .

## B. SOFIA/FORCAST FLUXES

RSGC1 is the only cluster with published SOFIA/FORCAST fluxes from another source. Comparison with the fluxes for the eight stars in common with RSGC1 in Beasor et al. (2020) shows that our aperture-based photometry is systematically lower with respect to their PSF measurements. The differences vary from star to star and with wavelength. They average  $\approx 0.1$  Jy for the two shortest wavelengths and up to  $0.5 - 0.6$  Jy  $\geq 11 \mu\text{m}$ .

**Table 11.** New SOFIA/FORCAST Photometry for Stars in NGC7419

Star	11.1 $\mu\text{m}$ (Jy)	31.5 $\mu\text{m}$ (Jy)	37.1 $\mu\text{m}$ (Jy)
NGC7419-B435	$1.53 \pm 0.25$	...	...
NGC7419-B696	$1.78 \pm 0.85$	$0.35 \pm 0.52^a$	...
NGC7419-B921	$1.24 \pm 0.78$	...	...
NGC7419-B950 <sup>b</sup>	$101.3 \pm 5.6$	$33.3 \pm 2.7$	$23.09 \pm 0.81$
		$41.1 \pm 2.9^a$	

<sup>a</sup>Level 4 data

<sup>b</sup>15''36 aperture diameter

**Table 12.** New SOFIA/FORCAST Photometry for Stars in RSGC1

Star	5.6 $\mu\text{m}$ (Jy)	7.7 $\mu\text{m}$ (Jy)	11.1 $\mu\text{m}$ (Jy)	25.3 $\mu\text{m}$ (Jy)	31.5 $\mu\text{m}$ (Jy)
RSGC1-01	$6.20 \pm 0.19$	$5.20 \pm 0.19$	$13.76 \pm 0.31$	$11.5 \pm 3.2$	$9.8 \pm 2.7$
RSGC1-02	$6.56 \pm 0.32$	$5.65 \pm 0.26$	$14.20 \pm 0.01$	$13.1 \pm 3.5$	$11.3 \pm 3.8$
RSGC1-03	$4.38 \pm 0.05$	$4.27 \pm 0.11$	$8.1 \pm 2.9$	$7.3 \pm 1.1$	$6.35 \pm 0.02$
RSGC1-04	... <sup>a</sup>	$2.43 \pm 0.11$	... <sup>a</sup>	$5.58 \pm 0.81$	$4.4 \pm 1.1$
RSGC1-05 <sup>b</sup>	$2.68 \pm 0.03$	$2.76 \pm 0.04$	$2.97 \pm 0.76$	$2.2 \pm 1.4$	$1.24 \pm 0.02$
RSGC1-06	$2.69 \pm 0.02$	$2.81 \pm 0.01$	$2.9 \pm 3.7$	$1.68 \pm 0.52$	$1.45 \pm 0.66$
RSGC1-07	$2.51 \pm 0.002$	$2.40 \pm 0.15$	$2.80 \pm 0.18$	$1.23 \pm 0.21$	$1.05 \pm 0.36$
RSGC1-08 <sup>b</sup>	$2.59 \pm 0.03$	$2.16 \pm 0.04$	$2.16 \pm 0.76$	$1.7 \pm 1.4$	$1.30 \pm 0.02$
RSGC1-09	$2.46 \pm 0.15$	$2.40 \pm 0.07$	$3.5 \pm 1.3$	$1.41 \pm 0.56$	$1.36 \pm 0.34$
RSGC1-10	$2.06 \pm 0.08$	$2.07 \pm 0.17$	$2.4 \pm 3.2$	$1.53 \pm 0.36$	$1.67 \pm 0.71$
RSGC1-11	... <sup>a</sup>	$1.92 \pm 0.05$	... <sup>a</sup>	... <sup>a</sup>	$1.14 \pm 0.27$
RSGC1-12	$1.64 \pm 0.07$	$1.61 \pm 0.12$	$1.8 \pm 1.4$	$1.18 \pm 0.07$	$0.53 \pm 0.91$
RSGC1-13	$3.92 \pm 0.31$	$3.02 \pm 0.01$	$7.04 \pm 0.83$	$7.17 \pm 0.68$	$7.6 \pm 1.4$
RSGC1-15	$1.025 \pm 0.002$	$0.465 \pm 0.002$	...	...	...

<sup>a</sup>Outside FOV

<sup>b</sup>RSGC1-05 and RSGC1-08 are merged. One 15.36'' aperture was fit around both stars to obtain a total flux. The ratios of their peaks were applied to this total value to determine approximate individual flux values.

REFERENCES

Alexander, M. J., Kobulnicky, H. J., Clemens, D. P., Jameson, K., Pinnick, A. & Pavel, M. 2009, *AJ*, 137, 6

Beasor, E. R. & Davies, B. 2016, *MNRAS*, 463, 1269

Beasor, E. R. & Davies, B. 2018, *MNRAS*, 475, 55

Beasor, E.R. Davies, B., Smith, N., van Loon, J. Th., Gehrz, R. D. & Figer, D. F. 2020, *MNRAS*,

Beauchamp, A. Moffat, A. F. J., & Drissen, L. 1994, *ApJS*, 93, 187

Benjamin, R. A., Churchwell, E, Babler, B. L., et al. 2003, *PASP*, 115, 953

**Table 13.** New SOFIA/FORCAST Photometry for Stars in RSGC2

Star	7.7 $\mu\text{m}$	11.1 $\mu\text{m}$	19.7 $\mu\text{m}$	25.3 $\mu\text{m}$	31.5 $\mu\text{m}$	37.1 $\mu\text{m}$
	(Jy)	(Jy)	(Jy)	(Jy)	(Jy)	(Jy)
RSGC2-02 <sup>b</sup>	$6.64 \pm 0.40$	$20.1 \pm 1.0$	$15.70 \pm 0.12$	$11.34 \pm 0.30$	$8.20 \pm 0.06$	$5.79 \pm 0.05$ $5.7 \pm 1.9$ $5.77 \pm 0.22^{\text{a}}$
RSGC2-03	... <sup>c</sup>	... <sup>c</sup>	... <sup>c</sup>	$1.15 \pm 0.71$	$0.95 \pm 0.02$	$0.67 \pm 0.52$ $0.69 \pm 0.45^{\text{a}}$
RSGC2-06	$1.25 \pm 0.38$	$1.32 \pm 0.43$	$0.66 \pm 0.05$	$0.31 \pm 0.17$	...	...
RSGC2-08	$0.62 \pm 0.39$	$0.84 \pm 0.08$	$0.3 \pm 1.1$	$0.67 \pm 0.33$	$0.57 \pm 0.56$	...
RSGC2-10	$0.84 \pm 0.52$	...	...	...	...	...
RSGC2-11	$1.24 \pm 0.61$	$1.23 \pm 0.99$	...	...	...	...
RSGC2-14	$0.58 \pm 0.53$	...	...	...	...	...
RSGC2-15	$0.68 \pm 0.01$	...	...	...	...	...
RSGC2-18	$0.28 \pm 0.70$	...	...	...	...	...
RSGC2-52	... <sup>c</sup>	... <sup>c</sup>	... <sup>c</sup>	...	...	$0.91 \pm 0.20$ $0.94 \pm 0.16^{\text{a}}$

<sup>a</sup>Level 4 data<sup>b</sup>15''36 aperture diameter<sup>c</sup>Outside FOV**Table 14.** New SOFIA/FORCAST Photometry for Stars in RSGC3

Star	5.6 $\mu\text{m}$	7.7 $\mu\text{m}$	11.1 $\mu\text{m}$	25.3 $\mu\text{m}$	31.5 $\mu\text{m}$
	(Jy)	(Jy)	(Jy)	(Jy)	(Jy)
RSGC3-01	$1.43 \pm 0.30$	$0.95 \pm 0.22$	...	...	...
RSGC3-02	... <sup>a</sup>	$0.77 \pm 0.24$	...	...	...
RSGC3-04	... <sup>a</sup>	$1.70 \pm 0.009$	...	...	...
RSGC3-05	$1.65 \pm 0.10$	$1.29 \pm 0.14$	...	...	...
RSGC3-06	$0.87 \pm 0.0004$	$0.31 \pm 0.002$	...	...	...
RSGC3-07	$0.96 \pm 0.61$	$0.59 \pm 0.15$	$1.22 \pm 0.56$	...	...
RSGC3-10	$0.73 \pm 0.28$	$0.37 \pm 0.11$	...	...	...
RSGC3-A11 <sup>b</sup>	$0.59 \pm 0.32$	$0.35 \pm 0.16$	...	...	...
RSGC3-27	... <sup>a</sup>	$0.17 \pm 0.20$	...	...	...

<sup>a</sup>Outside FOV<sup>b</sup>No cross-ID number in Clark et al. (2009)



- Cardelli, J. A., Clayton, G. C. & Mathis, J. S. 1989, *ApJ*, 345, 245
- Cassarà, L. P., Piovani, L., Weiss, A., et al. 2013, *MNRAS*, 436, 2824
- Clark, J. S., Negueruela, I., Davies, B., et al. 2009, *A&A*, 498, 1
- Davies, B., Figer, D. F., Kudritzki, R.-P. et al. 2007, *ApJ*, 671, 781
- Davies, B., Figer, D. F., Law, C. J. et al. 2008, *ApJ*, 676, 1016
- Davies, B., et al. 2013, *ApJ*, 767, 3
- Davies, B. & Beasor, E. R. 2018, *MNRAS*, 474, 2116
- Davies, B. & Beasor, E. R. 2019, *MNRAS*, 486, L10
- Decin, L., Honig, S., de Koter, A. et al. 2006, *A&A*, 456, 549
- de Jager, C., Nieuwenhuijzen, H. & Van Der Hucht, K. 1988, *A&AS*, 72, 259
- Egan, M. P., Price, S. D., & Gugliotti, G. 2001, *BAAS*, 34, 561
- Ekstrom, S., et al., 2012, *A&A*, 537, A146
- Elias, J.H., Frogel, J. A. & Humphreys, R. M. 1985, *ApJS*, 57, 91
- Fawley, W. M. & Cohen, M. 1974, *ApJ*, 193, 367
- Figer, D. F., MacKenty, J. W., Robberto, M. et al. 2006, *ApJ*, 643, 1166
- Gail, H.-P., Wetzell, S., Pucci, A., et al. 2013, *A&A*, 555, A119
- Gordon, M. S., Humphreys, R. M., Jones, T. J. et al. 2018, *AJ*, 155, 212 (Paper II)
- Hinz, P. M., Defrère, D., Skemer, A., et al. 2016, *Proc. SPIE*, 990704
- Humphreys, R. M. 1979, *ApJ*, 231, 384
- Humphreys, R. M. et al. 1997, *AJ*, 114, 2778
- Humphreys, R. M. et al. 2006, *AJ*, 131, 2105
- Ivezic, Z. & Elitzur, M. 1997, *MNRAS*, 287, 799
- Joshi, H., Kumar, B., Singh, K. P., et al. 2008, *MNRAS*, 391, 1279
- Koorneef, J. 1983, *A&A*, 128, 84
- Koumpia, E. et al. 2020, *A&A*, 635, A183
- Marco, A. & Negueruela, I. 2013, *A&A*, 552, 92
- Mathis, J. S., Rimpl, W., & Nordsieck, K. H. 1977, *ApJ*, 217, 425
- Mauron, N. & Josselin, E. 2011, *A&A*, 526, A156
- Murakami, H., Baba, H., Barthel, P., et al. 2007, *PASJ*, 59, S369
- Negueruela, I., Marco, A., Gonzalez-Fernandez, C., et al. 2012, *A&A*, 547, A15
- Negueruela, I., Gonzalez-Fernandez, C., Dada, R. et al. 2013, *Betelgeuse Workshop*, EAS Publications, 60
- Nieuwenhuijzen, H. & de Jager, C. 1990, *A&A*, 231, 134
- Ossenkopf, V., Henning, T. & Mathis, J. S. 1992, *A&A*, 261, 567
- Ramirez Alegria, S., Marin-Franch, A., & Herrero, A. 2012, *A&A*, 541, A75
- Reimers, D. 1975, *Mem. Soc. R. Sci. Liege*, 8, 369
- Rowan-Robinson, M., & Harris, S. 1982, *MNRAS*, 200, 197
- Shenoy, D. P., Jones, T. J., Humphreys, R. M., et al. 2013, *AJ*, 146, 90
- Shenoy, D., Jones, T. J., Packham, C., & Lopez-Rodriguez, E. 2015, *AJ*, 150, 15
- Shenoy, D., Humphreys, R. M., Jones, T. J., et al. 2016, *AJ*, 151, 51 (Paper I)
- Skrutskie, M. F., Cutri, R. M., Stiening, R., et al. 2006, *AJ*, 131, 1163
- Skrutskie, M. F., Jones, T., Hinz, P., et al. 2010, *Proc. SPIE*, 7735, 77353H
- Smartt, S. J. 2009, *ARA&A*, 47, 63
- Smartt, S. J. 2015, *PASA*, 32, e016
- Stephenson, C.B. 1990, *AJ*, 99, 1867
- Subramanian, A., Mathew, B., Bhatt, B. C. & Ramya, S. 2006, *MNRAS*, 370, 743
- Suh, K.-W. 2002, *MNRAS*, 332, 513
- Tiffany, C., Humphreys, R. M., Jones, T. J., & Davidson, K. 2010, *AJ*, 140, 339
- Verheyen, L., Messineo, M. & Menten, K. M. 2012, *A&A*, 541, A36
- Van Loon, J. T., Gronenewegen, M. A. T., de Koter, A. 1999, *A&A*, 351, 559
- Van Loon, J.T., Cioni, M.-R., Zijlstra, A. A., & Loop, C. 2005, *A&A*, 438, 273
- Wright, E. L., Eisenhardt, P. R. M., Mainzer, A. K., et al. 2010, *AJ*, 140, 1868